Morphology Evolution in Dealloying

by

Qing Chen

A Dissertation Presented in Partial Fulfillment
of the Requirements for the Degree
Doctor of Philosophy

Approved February 2013 by the
Graduate Supervisory Committee:

Karl Sieradzki, Chair
Daniel Buttry
Candace Chan
Cody Friesen

ARIZONA STATE UNIVERSITY

May 2013

ABSTRACT

Dealloying, the selective dissolution of an elemental component from an alloy, is an important corrosion mechanism and a technological significant means to fabricate nanoporous structures for a variety of applications. In noble metal alloys, dealloying proceeds above a composition dependent critical potential, and bi-continuous structure evolves “simultaneously” as a result of the interplay between percolation dissolution and surface diffusion.

In contrast, dealloying in alloys that show considerable solid-state mass transport at ambient temperature is largely unexplored despite its relevance to nanoparticle catalysts and Li-ion anodes. In my dissertation, I discuss the behaviors of two alloy systems in order to elucidate the role of bulk lattice diffusion in dealloying. First, Mg-Cd alloys are chosen to show that when the dealloying is controlled by bulk diffusion, a new type of porosity - negative void dendrites will form, and the process mirrors electrodeposition. Then, Li-Sn alloys are studied with respect to the composition, particle size and dealloying rate effects on the morphology evolution. Under the right condition, dealloying of Li-Sn supported by percolation dissolution results in the same bi-continuous structure as nanoporous noble metals; whereas lattice diffusion through the otherwise “passivated” surface allows for dealloying with no porosity evolution. The interactions between bulk diffusion, surface diffusion and dissolution are revealed by chronopotentiometry and linear sweep voltammetry technics.

The better understanding of dealloying from these experiments enables me to construct a brief review summarizing the electrochemistry and morphology aspects of dealloying as well as offering interpretations to new observations such as critical size

effect and encased voids in nanoporous gold. At the end of the dissertation, I will describe a preliminary attempt to generalize the morphology evolution "rules of dealloying" to all solid-to-solid interfacial controlled phase transition process, demonstrating that bi-continuous morphologies can evolve regardless of the nature of parent phase.

ACKNOWLEDGMENTS

I could not owe more thanks to my advisor, Dr. Karl Sieradzki, for his mentoring and help throughout my four years in the group. He equipped me with valuable knowledge, skills and attitudes that will always be helpful and guiding me in my academic journey. No matter what direction I will head for, he has made this trip a big appreciation of mine that I will cherish forever.

I would like to thank Dr. Cody Friesen, Dr. Dan Buttry and Dr. Candace Chan, from whom I never fail to learn. My labmates Xiaoqian Li, Shaofeng Sun and Elise Switzer have been great companies to my research and life. I'm also grateful that I can always receive supports from guys around like Nilesh Badwe, Toni Tang, Jose Bautista, Erika Engstrom, Jordan Kennedy, Qian Cheng, Andrew Brown and many others I regrettably can't list all.

My acknowledgements are also directed to Dr. Peter Crozier for his assistance to the TEM work, and Dr. Pedro Peralta for serving in my comprehensive committee. There are so many faculty and staff I've interacted with, without the help of whom I wouldn't be able to accomplish all my work.

At last, and above all, I would like to thank my parents back in China, for their unconditional love and support.

TABLE OF CONTENTS

Page

CHAPTER Page

LIST OF TABLES

LIST OF FIGURES

Figure Page

Figure Page

Figure Page

1 INTRODUCTION

Components in an alloy can be selectively dissolved owing to the chemical property difference, a process long known as dealloying. Research on dealloying dates back to the 1920s(*1*, *2*), when people were more concerned about its role in alloy corrosion. Dealloying process, if present, will determine an alloy's corrosion resistance, therefore various systems were examined with respect to their electrochemical responses, either for the alloy's practical importance, such as Zn-Cu and Al-Cu, or for its simplicity like Ag-Au and Cu-Au(*3*–*5*). Dealloying is also considered the cause for certain types of stress corrosion cracking, because the dealloyed layer is mechanically weak and injects crack into the alloy(*6*, *7*). This layer, owing to the development of characterization tools, was later observed to be beautifully nanoporous, and the porous structure is bi-continuous meaning that both the void space and the solid ligaments are continuous throughout the whole material (see Figure 1.1 for examples). This observation quickly shifted the center of dealloying research towards its more desirable role in nanostructure fabrication. Because of its high surface area and metallic nature, the dealloyed structure is attracting more attention in a wide range of applications, including catalysts(*8*), sensors(*9*), actuators(*10*), and radiation damage resistant materials (*11*).

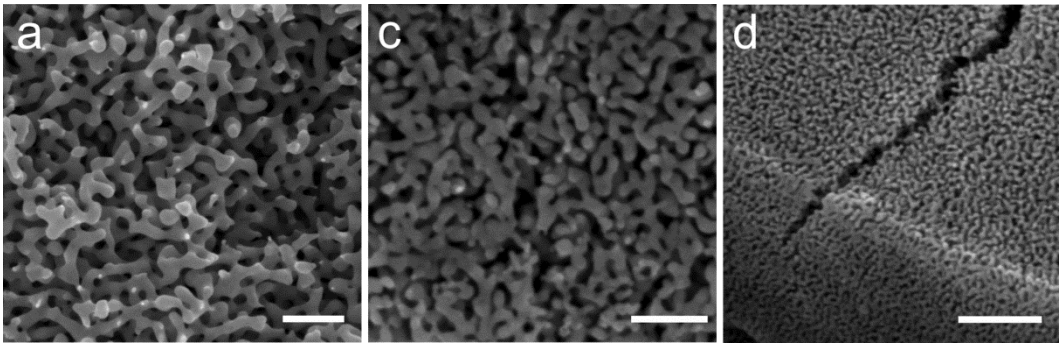

Figure 1.1 Nanoporous metals prepared by dealloying (a) Ag-Au, (b) Mn-Cu and (c) Stainless steel 316. The scale bars are 200 nm

1.1 Bi-continuous structure, critical potential and parting limit

These are the three key features accompanying dealloying. As mentioned earlier, the bi-continuous porous structure evolves naturally during dealloying. The ligaments are composed mainly by the more noble component, and their diameter, ranging from a few nanometers to micrometers; controllable either in-situ (during dealloying) or by post-annealing(*12*).

The other two features can be best seen in polarization curves. These curves are either obtained by simply sweeping the potential from low to high, or constructed by obtaining the steady-state current density at fixed potentials(*13*). Fig. 1.2 is a typical plot of a group polarization curves for different Ag-Au alloys. Ag-Au has always been the most popular system for dealloying study, due to its simplicity. This simplicity includes the full composition range of solid solution phase, the large difference in the standard potential of Ag and Au, and the relatively simple electrochemistry of both components in aqueous electrolyte. As shown in Fig. 1.2, compared to pure less noble metal's dissolution potential (0 mV), dealloying always turns-on at a much higher overpotential, which is the so-called critical potential. Below this potential, dealloying is usually limited to a thin

surface layer(*14*), and above it, dealloying behaves qualitatively like elemental metal dissolution but results in bi-continuous structures. The value of critical potential cannot be explained by the activity of the less noble component in the alloy, which comprises only a very small portion of the overpotential with respect to the standard potential of the element dissolving. The critical potential also increases with decreasing less noble component content, until reaching an alloy composition for which dealloying can no longer proceed. This lower bound of less noble component content for dealloying is termed as parting limit. For Ag-Au, this parting limit is about 55 at% Ag(*4*).

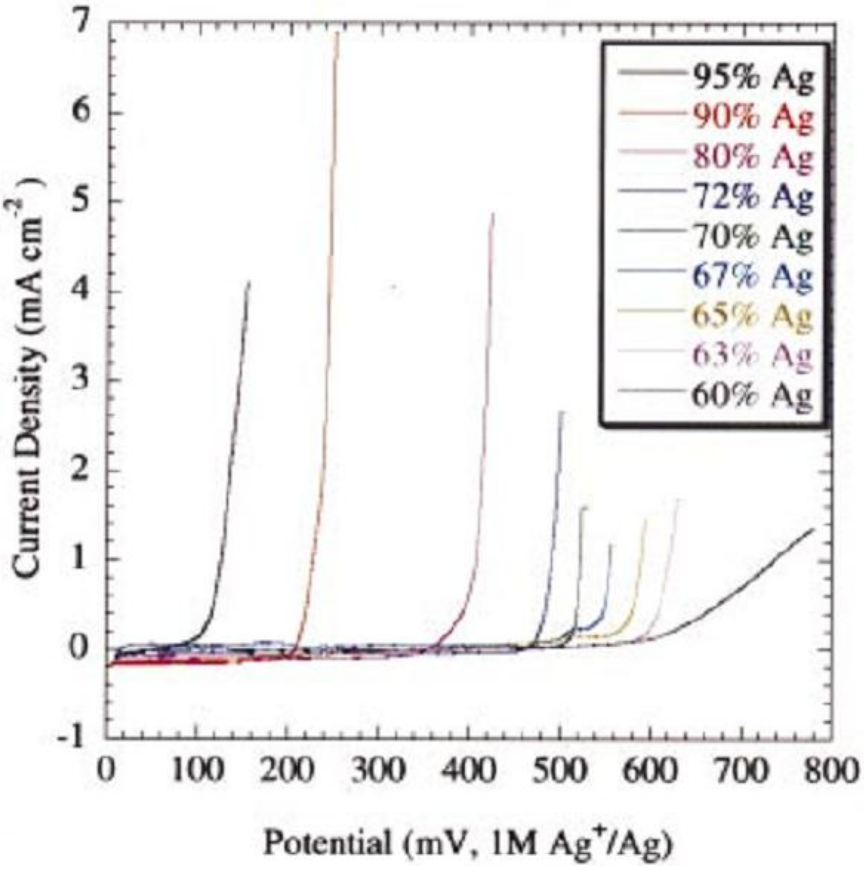

Figure 1.2 Polarization curves of Ag-Au alloys in 1 M AgClO4 +1 M HClO4 solution (*4*). The curves from low to high voltage are in the exact same sequence as for increasing Ag contents. The scan rate is 1 mV/s

1.2 History of dealloying mechanisms

To explain the kinetics behind dealloying has always been a complicated but fascinating task. Various mechanisms have been proposed, and are summarized with the drawings in Fig. 1.3 and 1.4. The model eliminated most easily is "dissolution and re-deposition". It proposes that during dealloying both components of a binary alloy are dissolving simultaneously and the more noble component re-deposits in a form of porous structure. This speculation can be tested by a rotating-ring-disk electrode (RRDE) experiment, which was conducted by Pickering and Wagner in 1967(*15*). They used a Cu-Au alloy as the disk and during its dealloying no Au reduction was detected on the Pt ring.

In the same work, Pickering and Wagner proposed another possible mechanism of dealloying based on solid-state bulk diffusion. Under this mechanism, the more noble component builds up a surface layer isolating the dissolving component from the electrolyte, and dealloying needs to proceed by bulk diffusion through the layer. However, mono-vacancy diffusion in all examined alloy systems is too slow by tens of orders of magnitudes to support dealloying(*16*). Therefore, they turned to a bulk diffusion path via di-vacancies. This type of diffusion usually happens at relatively high homologous temperature (T_H, experimental temperature divided by metal or alloy melting point), so an associated assumption was that large amount surface vacancies from dealloying would be injected to the bulk to facilitate the bulk diffusion. Regardless of the validity of this controversial assumption, the bulk diffusion flux calculated was still orders lower than that measured in dealloying. Moreover, to achieve 1 $mAcm^{-2}$ current density which is

routinely obtained during dealloying of Cu-Au and Ag-Au, the surface mole fraction of di-vacancy needs to unrealistically approach 1. All the key dealloying features discussed in the previous session cannot be explained by this mechanism either - especially the morphology. As shown in Fig. 1.3b, if the dealloying is carried out by bulk diffusion, the alloy surface will develop wedges later turned into "trees" but with no connectivity to each other.

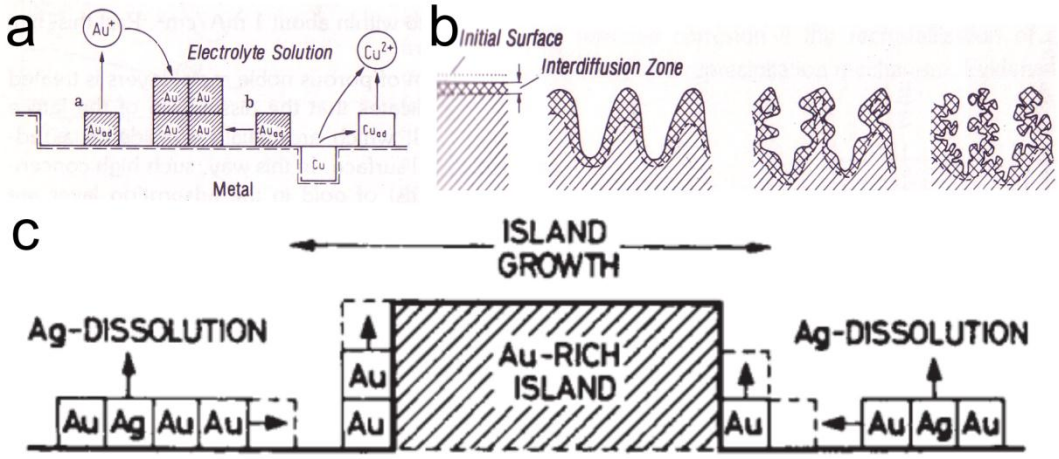

Figure 1.3 Cartoons of dealloying mechanisms for (a) dissolution and re-deposition (Cu-Au), (b) solid-state bulk diffusion(*17*), and (c) surface diffusion (Ag-Au)(*18*)

On the other hand, atoms on the surface have no difficulty diffusing around. In fact, the dealloying process must involve a high degree of surface diffusion for its production of a large number of adatoms and atoms at defect sites, or phrased in the larger scale, features with high curvature that need to be smoothened to lower the surface energy. The clear correlation between surface diffusion and the dealloying morphology was established when Forty(*18*) reported for the first time bi-continuous structures by dealloying Ag-Au alloy. In the work, he characterized the morphology evolution along with increasing dealloying time and post-annealing time, showing that the 2-dimentional

"maze"-like islands enlarge at their edges into an interconnected network. Based on this observation, he suggested a surface diffusion controlled mechanism illustrated in Fig. 1.3c. The dealloying starts with surface Ag dissolution, leaving Au atoms diffusing into growing Au island; this surface diffusion process in turn exposes more Ag to the electrolyte, which advances the dissolution layer by layer. This scenario successfully visualizes the morphology evolution during dealloying and becomes a basis for the understanding of dealloying.

However, with surface diffusion alone, it is difficult to give quantitative or even intuitive explanations to dealloying features like critical potential and parting limit. The piece missing is to describe the alloy at the moment right before the dissolution, when both types of atoms are still in the matrix, because the atom neighbors will definitely affect the probability of a specific dissolution event. This problem was solved when percolation theory was introduced by the works of Sieradzki and Newman(*19*, *20*). As far as dealloying in noble metal alloys is concerned, the percolation theory is capable of explaining most observations, and will also be the base of my dissertation.

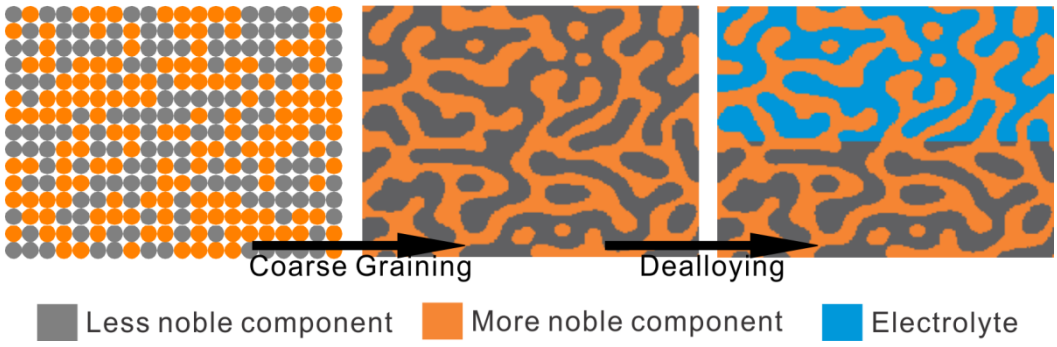

Figure 1.4 Illustration of the dealloying theory based on percolation

To apply percolation theory to dealloying, we start with a close-to-ideal binary solid solution alloy A_pB_{1-p}. The bulk material can be viewed as two types of atoms randomly distributed inside a crystal matrix. As percolation theory states, once a component's content is above a percolation threshold (p_c), the atoms of the same kind will form continuous clusters via near neighbor bonding throughout the whole material(*21*). Therefore when p is above p_c, the clusters of less noble component A will serve as the pathways for electrolyte to follow which sustains the dissolution, and $p=p_c$ sets the ground for the parting limit. When 1-p is above p_c, the remaining B clusters become the continuous backbone for the evolving porous structure. The average A cluster size will be composition dependent. Small as it always is, the cluster's dissolution requires an extra overvoltage from the associated Gibbs-Thompson term, and this is reflected in the magnitude of the critical potential(*4*, *22*). Although in most cases, surface diffusion causes the real dealloying process to deviate from the ideal prediction, the three key features of dealloying are well explained collectively by the mechanism in systems like Ag-Au(*4*, *22*).

1.3 State-of-the-art of dealloying research

The present picture of dealloying related research can be roughly drawn by constructing a citation report of a 2001 paper titled "Evolution of nanoporosity in dealloying"(*23*), which is the most cited paper on the topic. As shown in Fig. 1.5, while the alloy corrosion part of dealloying remains steady over the years, the total number of citations increases exponentially owing to the increasing interests in the nanostructures. One major contributor is catalysis research, which at the year of 2012 made up more than

one third of the overall citations. Among these exist two main directions with quite different concerns: one is using the process to achieve high surface area(*8*, *24*); the other is applying the theory to explain the instability of alloy catalysts(*25*), which can, though rarely, be categorized as alloy corrosion.

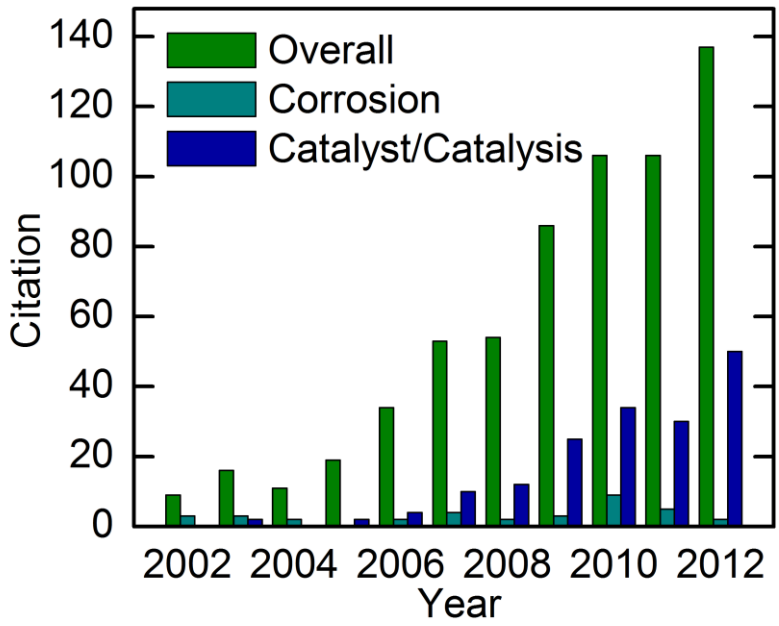

Figure 1.5 Statistics of the citation number for "Evolution of nanoporosity in dealloying". For the corrosion part, only publications from electrochemical journals (such as *J. Electrochem. Soc.* and *Corr. Sci*.) are included to roughly eliminate those applying the corrosion process for nanostructure fabrication. All data is from Web of Science

The types of alloys undergoing the most studies are still those containing at least one noble metal component. To obtain nanoporous structures, base metals such as Al(*26*), Ni(*8*) and Co(*27*) are often chosen as the dissolving species to reduce costs; multiphase alloys(*28*), nonequilibrium alloys(*29*) and amorphous alloys(*30*) have also been studied to broaden the applicability of this synthesis process. The most popular more noble component for dealloying is undoubtedly Pt, due to its supreme catalytic ability towards

various reactions such as oxygen reduction(*8*). At the same time as precious metals' prices soar, downsizing the alloy electrodes becomes a major trend of dealloying. This gives rise to a group of new morphologies that are never seen in bulk electrodes, including core-shell structures and hollow structures(*27*, *31*).

Along with the experimental works, computer simulation is also playing a big role in dealloying research. The most common approach is Kinetic Monte Carlo (KMC), which was performed as early as 1980 by Sieradzki et al.(*19*) and then improved by the works of Erlebacher(*23*, *32–34*). The coding visualizes dissolution and surface diffusion processes, with controllable parameters like voltage and bonding energy, which is able to reproduce all the key features discussed in session 1.1. Meanwhile, because kinetic events during dealloying elapse too quickly to be captured experimentally, KMC has been a great complement for both analysis(*32*) and prediction(*35*). Other simulation tools are not so often employed, but have shown potentials towards specific problems in dealloying such as ligament stability(*36*) and surface dealloying(*37*).

All the extensive works discussed above are in systems that display negligible lattice diffusion at the experimental temperature, such as noble metal alloys at ambient temperauter. In contrast, dealloying of systems with considerable ambient solid-state diffusion remains virtually unexplored. It will be of fundamental interests to understand the role of bulk diffusion when it actively participates the dealloying. In addition, there are two practically significant issues tightly linked to this type of dealloying. The first issue is in nanoparticles of small enough size to involve melting point depression thus increasing bulk diffusivity(*38*, *39*). The second is with Li alloys, which are considered as future Li-ion anodes. In those alloys, the bulk diffusion process is known to be fast even

at room temperature(*40*), and surprisingly, there has yet been any comprehensive works with respect to morphology evolution and the electrochemical parameters affecting this process.

In this dissertation, I will first attempt to answer the question of how the bulk diffusion affects the dealloying process and its morphology evolution. In Chapter 2, the close-to-ideal Mg-Cd alloy system is explored to show that a new kind of morphology, i.e. negative void dendrite, evolves when dealloying is under bulk diffusion control. Chapter 3 is centered on Li containing alloys. Depending on the alloy composition, electrode size and dealloying rate, bi-continuous structures evolve as well as other known dealloying morphologies. Based on the works in Chapter 2 and 3, and all the contributions from colleagues to dealloying research, a brief review will be constructed with the focus on electrochemical behaviors and morphology evolution of dealloying across all the alloy systems examined to date. At last, Chapter 5 presents initial efforts to extend the theory of dealloying beyond purely metallic systems, by showing the bi-continuous structure can evolve in any interfacial controlled selective dissolution process.

2 SOLID-STATE MASS TRANSPORT CONTROLLED DEALLOYING IN MG-CD ALLOYS

2.1 Background

As mentioned in the previous chapter, solid-state bulk diffusion was initially considered as one possible mechanism to support ambient temperature dealloying. Following an approach analogous to that adopted by Wagner in developing analytical models for high temperature oxidation(*41*), Pickering and Wagner developed a model of ambient temperature dealloying of Zn-Cu and Cu-Au alloys by assuming that diffusion was supported by a di-vacancy mechanism(*15*). In order to account for the experimentally measured large dealloying fluxes, they had to assume the existence of abnormally high concentrations of excess di-vacancies during dealloying, for instant, a mole fraction of di-vacancies of order 10^{-2} for a dealloying current density of 10^{-4} Acm^{-2}, and of order 1 for 10^{-3} Acm^{-2}. These current densities and higher are easily obtained, and we note that the alloy compositions considered by these authors were already above percolation thresholds therefore solid-state mass transport was not required for dealloying these systems. There are other works where dealloying were carried out under conditions of significant bulk diffusion, including Ag-Au alloys at 800C(*42*) and In-Sn alloys at room temperature(*43*), but the lack of characterization tools greatly limited their completeness.

In order to address the issue of morphology evolution in an alloy when the rate-limiting step (RLS) for dealloying is solid-state mass transport it will be necessary to consider two conditions with respect to alloy composition and elemental site occupation. First, as described in the introduction, for the case of single phase solid solution alloys

the composition of the dissolving species must be below the site percolation threshold of the lattice network, otherwise continuous nearest neighbor pathways are available to support dealloying. Second, in typical metal alloys where the lattice sites are almost fully occupied and the interstitial site occupation is dilute, the alloy component being dissolved must occupy the lattice sites in the crystal structure of the alloy. On a thermodynamic basis, for these alloys the interstitial components can be treated as "fluids" within the solid network in the sense that the dissolution or accretion of such a component from the surface leaves the number of lattice sites unchanged(*44*) and does not result in the creation of surface vacancy. In more complicated crystal structures where site occupancy for both the lattice and interstitial sites is high, the interstitial vacancies can be treated as solid components in a thermodynamic sense and dealloying could still result in vacancy creation(*45*). We briefly discuss one possible example at the end of this chapter.

The morphology evolution by bulk diffusion controlled dealloying can be discussed under the rule of phase transformation kinetics and interface stability to perturbations first identified by Wagner(*41*). This simple rule is applicable to a variety of "growth" processes including elemental metal and alloy solidification, oxidation, electropolishing and electrodeposition. Within the context of electrochemical dealloying consider the growing phase to be the electrolyte and the shrinking phase to be the parent phase alloy. If the rate-limiting step (RLS) is in the shrinking phase, a planar alloy/electrolyte interface will be unstable to perturbations that will tend to grow in magnitude as time evolves, whereas if the RLS is in the growing phase the planar interface will be stable. Consider an A_pB_{1-p} binary alloy in which A is the dissolving component and B is "insoluble" in the electrolyte. Figure 2.1 depicts the expected dealloyed morphologies at

compositions above and below the site percolation threshold of component A. Above the percolation threshold, even if the solid-state diffusivity of component A is large, dealloying will still be under interface control and the dealloyed morphology will be bi-continuous. At compositions below the percolation threshold selective dissolution of the A component can only proceed by a process involving the mass transport of A from the interior of the alloy to the alloy/electrolyte interface. For every A atom dissolved from a terrace site on the interface a vacancy is formed at that location. Such a dissolution process is isomorphic to a diffusion-limited aggregation (DLA) processes. Thus we expect to observe a dealloyed morphology consisting of negative tree-like structures or "void-dendrites" penetrating into the solid. In analogy with normal dendritic growth the detailed shape evolution of these negative dendrites will reflect the anisotropy in interfacial energy defined by the crystal lattice structure of the now dealloyed parent phase.

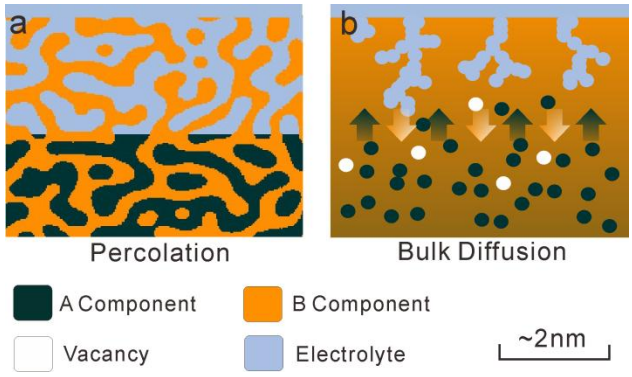

Figure 2.1 Mechanisms of dealloying (a) above and (b) below percolation threshold.

In this chapter, Mg-Cd alloy system is chosen for the following reasons. Unlike noble-metal-containing alloys, Mg-Cd alloys have relatively low melting points over the entire compositional range (Figure 2.2) which guarantee high bulk diffusion rates at or

near ambient temperatures. They form a series of hexagonal close packed (HCP) based structures that minimizes the crystal structure change during dealloying. In addition, the Mg-Cd system was one of the early systems for which the Kirkendall effect was examined so that there exists data for the chemical interdiffusion coefficients(*46*), which will helpfully guide our theoretical analysis.

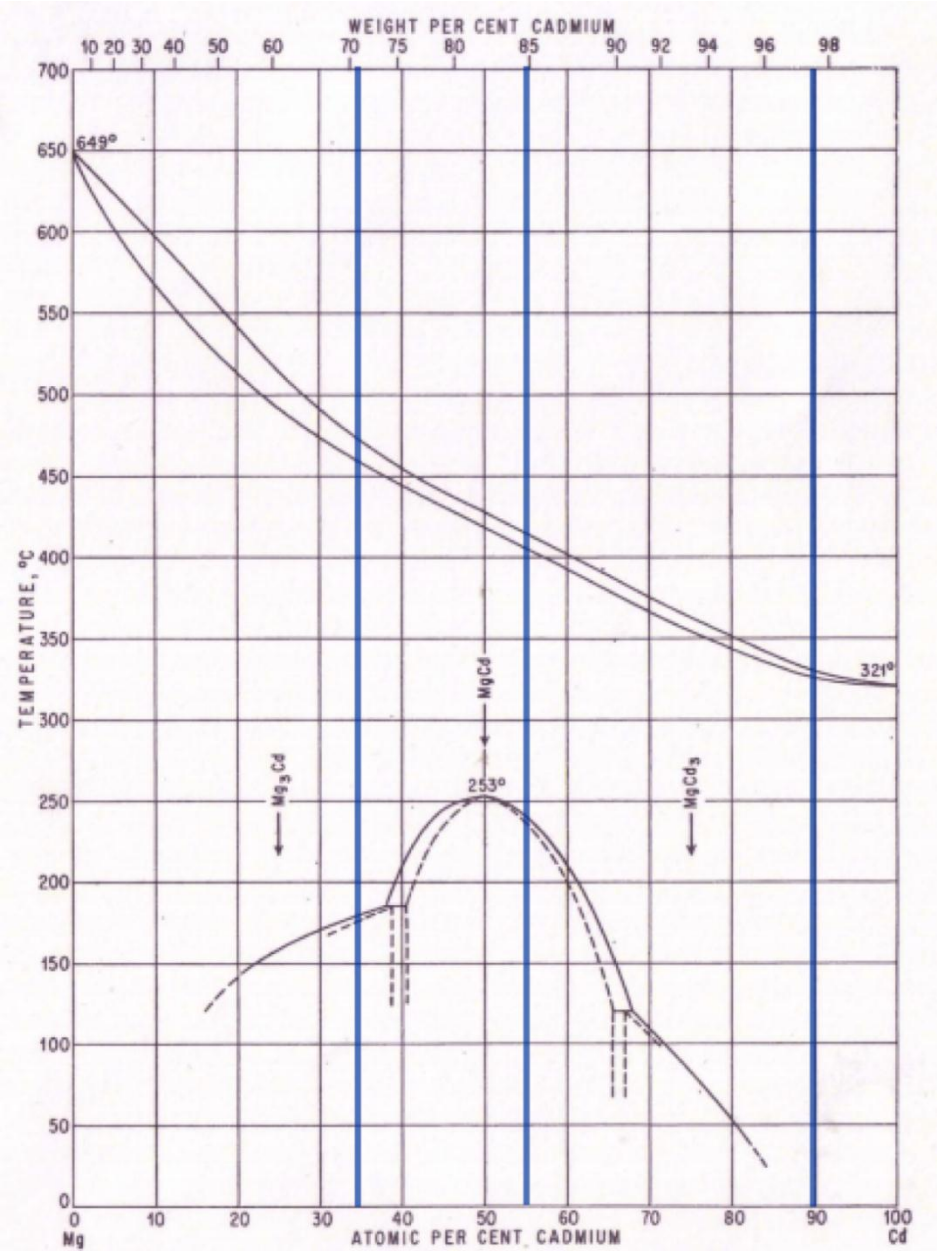

Figure 2.2 Mg-Cd phase diagram (with chosen compositions labeled)(*47*)

2.2 Experiments

Mg-Cd alloys were supplied by the Ames Laboratory. The three compositions (at %) used here are $Mg_{0.65}Cd_{0.35}$ ($D0_{19}$ structure; melting temperature, 743 K), $Mg_{0.45}Cd_{0.55}$ (B19 structure; melting temperature, 698 K) and $Mg_{0.10}Cd_{0.90}$ (random hcp structure; melting temperature, 613 K). Elemental Mg and Cd (99.9% purity) were purchased from Alfa Aesar. All electrodes were mechanically polished to 1200 grit with hexane as a lubricant, except $Mg_{0.10}Cd_{0.90}$, which was further electropolished in H_3PO_4-glycol-water (2:2:1 in volume ratio) solution(*48*).

The composition and crystal structure of the alloys were checked by X-ray Diffraction (XRD) and Energy Dispersive X-ray Spectroscopy (EDS). Wet chemical analysis was adopted to verify the EDS results.

Dealloying of Mg was performed in either Choline Chloride-Urea (ChCl-Urea) ionic liquid (iL) or 1-Butyl-3-MethylImidazoliumm bis-Trifluoromethylsulfonate (BMImTfSI). The ChCl-Urea was prepared by mixing ChCl (Alfa Aesar, 95+%) and Urea (EMD, 99%) in 1:2 molar ratio. Prior to the electrochemical experiments, both iLs were deaerated in an MBraun glovebox, until the water content was below 100 ppm for ChCl-Urea, and 1ppm for BMImTfSI (EMD), tested by Karl-Fischer titration (Mettler Toledo model C20).

The dealloying experiments were performed in an Ar-deaerated three-electrode cell using a Gamry Series G potentiostat. Platinum mesh was used as the counter electrode and a Cd wire, with pre-dissolved ~10^{-4} mol/L Cd^{2+} served as a pseudo reference electrode. The potential stability of this reference was ± 50mV over the duration of the

experiments. For all experiments dealloying was performed at -100mV vs. the reference electrode, for time periods ranging from 1000~10000s.

In the ancillary Kirkendall voiding experiment, a 500 nm thick layer of Cd, mimicking the dealloyed Cd-rich layer, was electrodeposited on to an electropolished $Mg_{0.10}Cd_{0.90}$ alloy surface from an aqueous electrolyte containing 0.1M $CdSO_4$ (Fluka, 99.9%) and 1mM NH_4OH (Sigma Aldrich, 28~30%). The sample was then annealed at 210 C ($T_H = 0.618$) for 10000 s in an atmosphere containing 5% H_2 + 95% Ar.

During Focused Ion Beam (FIB) cross-section milling, there was always a 100 to 500nm platinum layer deposited by the gallium ion beam to protect the top surface. The cross-section images were taken with a 52 degree angle versus the horizontal plane, meaning a ~1.62x correction to the depth-direction length measurement in the images.

FIB, Scanning Electron Microscopy (SEM) and EDS were all conducted in FIB/SEM Nova 200 NanoLab UHR FEG (FEI) system. XRD spectra were obtained by PANalytical X'Pert Pro Materials Research X-ray Diffractometer with a Cu Kα source. Electron Backscatter Diffraction (EBSD) experiments were performed in FEI XL30 SEM system.

2.3 $Mg_{0.65}Cd_{0.35}$ and $Mg_{0.45}Cd_{0.55}$ dealloying and bi-continuous structure formation

As a routine for all Mg-Cd alloys employed, EDS, XRD and electrochemical polarization were applied to verify alloy properties. In Figure 2.3, EDS and XRD results show both alloys are of the nominal composition and crystal structure; Figure 2.3e is a typical polarization curve for high Mg content alloy, whose oxidation potential sits between elemental Mg and Cd.

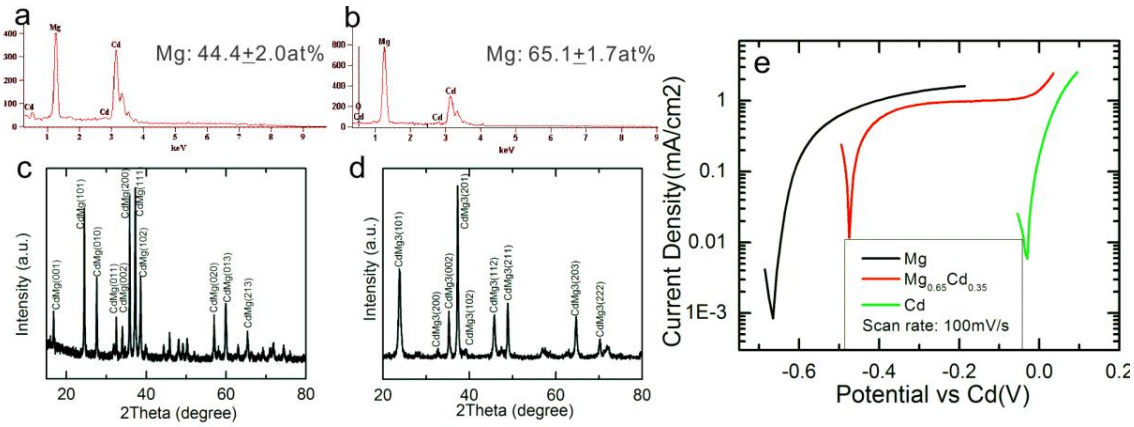

Figure 2.3 EDS, XRD and polarization data for (a, c, e) $Mg_{0.65}Cd_{0.35}$ and (b, d) $Mg_{0.45}Cd_{0.55}$

The reason why we used ChCl-Urea in high Mg content alloy dealloying is due to the existence of a robust oxide on the alloy surface. BMImTfSI is not able to dissolve it and the dealloying results in highly localized pits, whereas ChCl-Urea yields a clean dealloyed surface. After dealloying, the electrode surface was quickly washed with water and isopropanol. Both alloys' dealloying resulted in the evolution of uniform bi-continuous porous structures, as shown in Figure 2.4. The length scale of the bi-continuous morphology for the 65at% Mg alloy ranged from ~4 to 10 μm which is considerably larger than that found in the room temperature dealloying of noble face-centered cubic alloys such as Ag-Au(*12*). This larger length-scale is a result of the high homologous temperature (T_H ~0.50) at which these experiments were carried out. Consequently Ostwald ripening of the ligaments is significantly enhanced by surface mass-transport processes(*12*). The length scale of the bi-continuous morphology for the 45 at% Mg alloy is ~ 2 μm and at this composition there are no comparisons to be made to dealloying in noble FCC alloys as this composition is below the so-called parting limit

of such alloys(*19*). In fact to our knowledge, this is the first demonstration of bi-continuous porosity evolution in a binary alloy at this composition, and we will re-visit the concept of parting limit in Chapter 4.

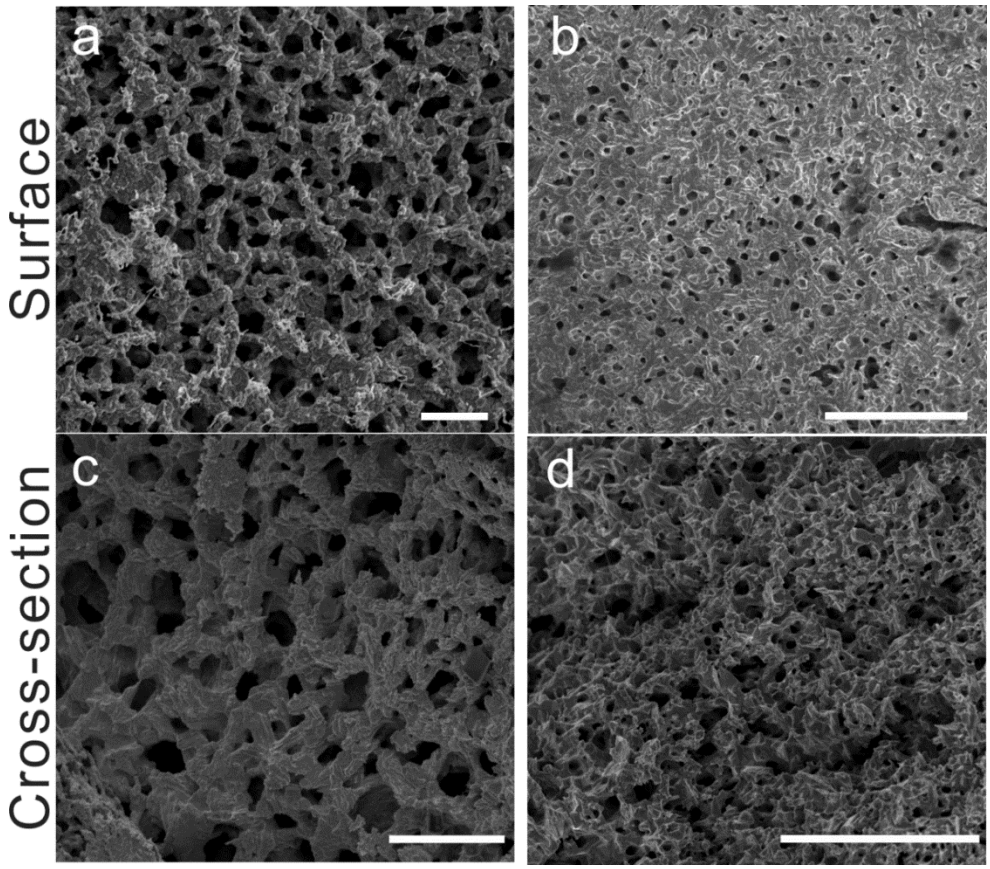

Figure 2.4 Dealloyed Morphologies of (a, c) $Mg_{0.65}Cd_{0.35}$ and (b, d) $Mg_{0.45}Cd_{0.55}$. The scale bars are 10 um

2.4 $Mg_{0.10}Cd_{0.90}$ dealloying and negative dendrite structure formation

As shown in Figure 2.5, $Mg_{0.10}Cd_{0.90}$ started with the designated composition, crystal structure and electrochemical property. For this alloy, dealloying was carried out in the in the BMImTfSI iL for three reasons. First this iL has a much higher decomposition temperature which allowed us to examine dealloying over a wider range in homologous

temperature. Second this iL has a larger electrochemical stability window and a thin cadmium-rich oxide film is preserved (retained from electropolishing) on the surface of this alloy that serves to sufficiently quench surface diffusion processes that might otherwise obscure or alter the dealloyed morphology. We note that the Mg content in this alloy is well below the 20 at% site percolation threshold for the hcp crystal structure(*49*).

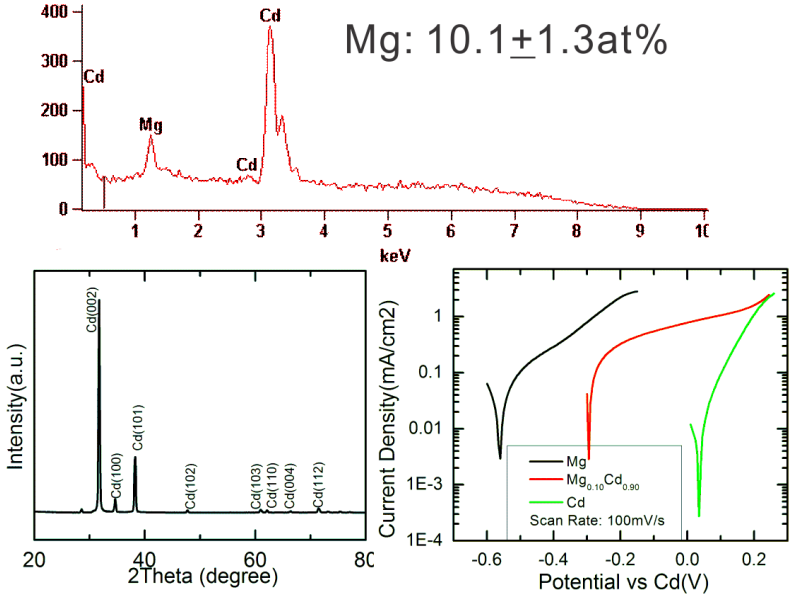

Figure 2.5 EDS, XRD and polarization data for $Mg_{0.10}Cd_{0.90}$

Figure 2.6 shows FIB cross-section images of the dealloyed morphologies in $Mg_{0.10}Cd_{0.90}$ at different dealloying temperatures, for varying times. At 50C (T_H = 0.527) it was difficult to discern dealloying features, which were likely too shallow in depth. At T_H = 0.690, significant DLA/dendrite-like structures are apparent owing to the higher Mg diffusivity. Unlike bi-continuous porous structures, the void-dendrite branches do not merge into one another. This is a consequence of the depletion in Mg that occurs in regions between the dendrites and the inability of significant amounts of Mg to diffuse

into these regions as the Mg diffusers are captured by the tips of the growing dendrites. In spite of significant coarsening, there is distinguishable side branching and accordingly some level of self-similarity to the morphology of these structures. At a temperature of T_H = 0.788, deeper growth is observed within the same period of time. At this temperature these structures coarsen more quickly and are consequently not as narrow, however, fractal-like features of this morphology are more apparent.

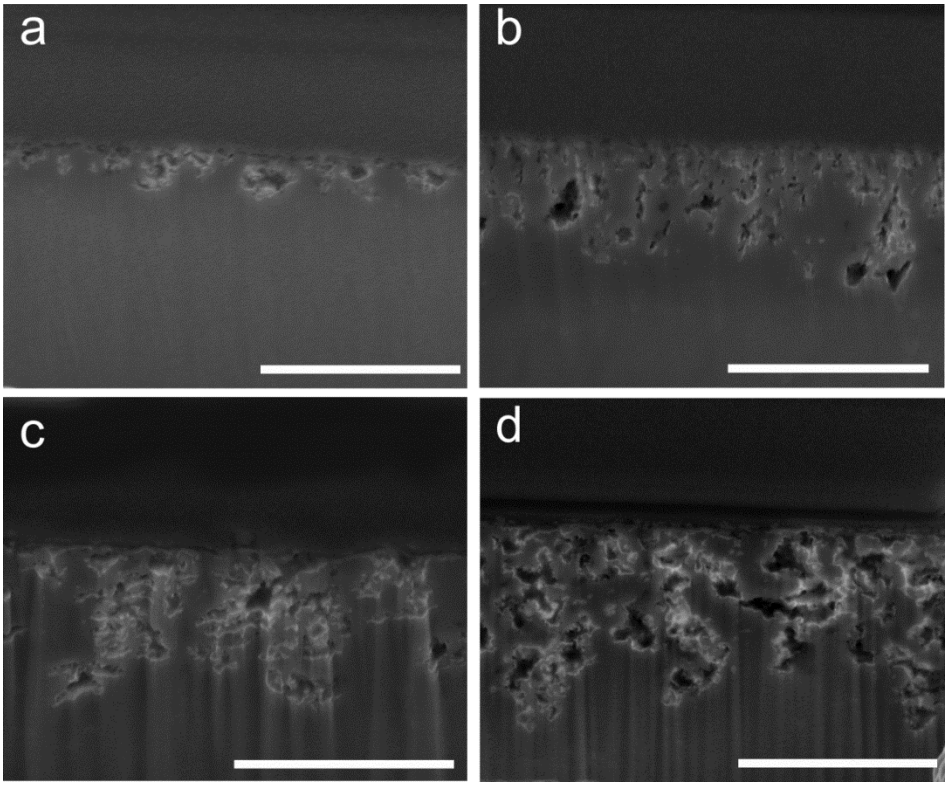

Figure 2.6 Cross-section views of $Mg_{0.10}Cd_{0.90}$ dealloyed at various conditions: (a) 50C for 10000s; (b) 150C for 10000s; (c) 210C for 5000s; (d) 210C for 10000s. The scale bars are 1um.

2.4.1 Grain orientation dependence of negative dendrites

Similar as positive dendrites by deposition, negative dendrites display preferential growth, rooted from the anisotropy of the parent alloy. Prior to dealloying Electron

Backscatter Diffraction (EBSD) was used to determine grain orientations in order to assess this issue. Figure 2.7 shows FIB-milled cross-sections of the dealloyed structures for three adjacent grains (orientations are indicated in Figure 2.7a, with colors corresponding to the Miller index in the sector plot).

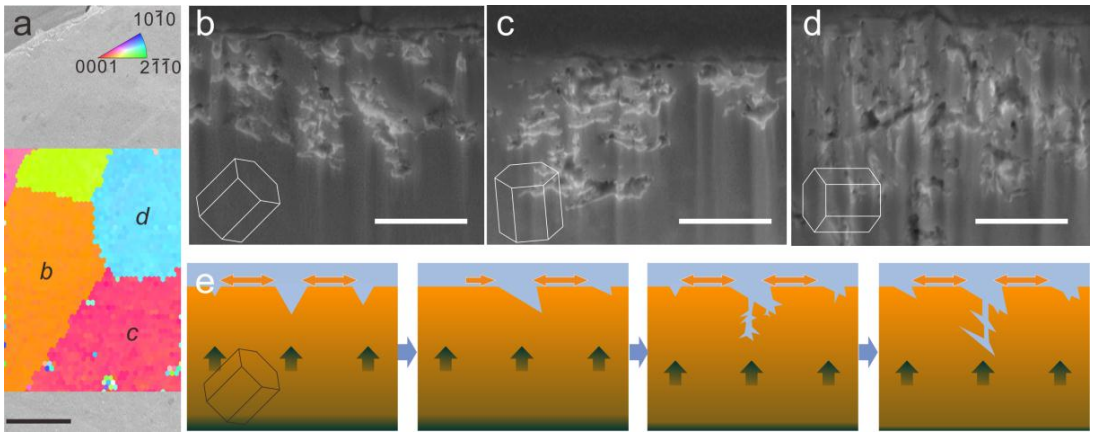

Figure 2.7 Correlation of EBSD results and negative dendrite morphologies obtained by dealloying the $Mg_{0.10}Cd_{0.90}$ alloy: (a) EBSD results for a section of the planar surface showing grain orientations by color indicated in the standard triangle. Scale bar 600um; (b-d) FIB milled cross-sections of the three grains labeled in a, with lattice orientations illustrated as insets. Scale bars are 400 nm. (e) Cartoon illustration of negative dendrite morphology evolution for the grain orientation shown in image b.

We observed that the dendrites were mainly aligned along the basal plane for each of the grain orientations. This is similar to the orientation-dependent pitting corrosion in Cd(*48*) and Mg(*50, 51*). Although the details of the kinetics of pitting and negative dendrite formation are different, we attribute our dendrite orientations to the same cause as that observed in the pitting corrosion of elemental Cd and Mg – the anisotropy of surface energy. In the hcp structure, the basal plane has the lowest surface energy(*52, 53*). The dendrite surface orientations evolve by surface diffusion and the driving force for this is the minimization of the interfacial energy. Figure 2.7C is an illustrative cartoon

showing how the combination of dealloying and surface diffusion acts to evolve these directionally anisotropic void-dendrite structures.

2.4.2 Current-time behavior for bulk diffusion limited dealloying

During dealloying, the measured current density follows $t^{-1/2}$ kinetics. Both the dealloyed morphology and the kinetics of dealloying provide strong evidence for solid-state mass transport control of dealloying at the $Mg_{0.10}Cd_{0.90}$ alloy composition. Evaluation of the growth rate of these DLA-like structures from the measured current-time behavior is exceptionally complex, as this is a fully non-linear three-dimensional diffusion problem and likely only amenable to solution using numerical techniques. Nevertheless, considerable insight can be drawn from a simple one-dimensional solution incorporating a moving alloy/electrolyte boundary.

Following Pickering and Wagner(*15*) we consider diffusion normal to the initial alloy/electrolyte interface and at time zero that the initial concentration of Mg, c_0 (mol/cm^3), is uniformly distributed within the bulk of the alloy. The flux of Mg atoms at the instantaneous position, z_i of the interface is given by $J = D(\partial c/\partial z)_{z=z_i}$, and the concentration of Mg atoms at the interface is taken to be zero. The interface velocity given by

$$\mathrm{d}z_i/\mathrm{d}t = V_m D(\partial c/\partial z)_{z=z_i} \qquad 2\text{-}1$$

where V_m is the molar volume of Mg in the alloy and D is the diffusivity. Under the stated initial and boundary conditions a solution to the time dependent diffusion equation

$$\frac{\partial c}{\partial t} = D\frac{\partial^2 c}{\partial z^2} \qquad 2\text{-}2$$

is given by,

$$z_i = 2\alpha(\mathrm{Dt})^{1/2} \qquad 2\text{-}3$$

$$c = c_0(1 - \mathrm{erfc}\,(\tfrac{z}{2(\mathrm{Dt})^{1/2}})/\mathrm{erfc}\,\alpha) \qquad 2\text{-}4$$

where α is a constant determined by substitution of Equation 2-3 and 2-4 into Equation 2-2 as

$$\pi^{1/2}\alpha\ \mathrm{erfc}\alpha\ e^{\alpha^2} = p \qquad 2\text{-}5$$

The magnitude the A flux at the instantaneous position of the alloy/electrolyte interface is given by,

$$J = D(\partial c/\partial z)_{z=z_i} = \frac{c_0 e^{-\alpha^2}}{\mathrm{erfc}\alpha}(\frac{D}{\pi t})^{1/2} \qquad 2\text{-}6$$

and the dealloying current density is

$$i = 2JF = 2F\frac{p}{V_m}\frac{e^{-\alpha^2}}{\mathrm{erfc}\alpha}(\frac{D}{\pi t})^{1/2} \qquad 2\text{-}7$$

For the alloy compositions considered by Pickering and Wagner, *p* was near unity and consequently they employed a series expansion for the *erfc* function in order to determine α. For the composition (p = 0.1) of interest here we evaluate α numerically from Equation 2-5 to be 0.06. Then we obtain,

$$i = 2.15F\frac{p}{V_m}(\frac{D}{\pi t})^{1/2} \qquad 2\text{-}8$$

This analysis assumes that the chemical diffusivity is independent of composition over the relevant range in Mg concentration (0~10 at%). We have fit the current decays to this form of the current density and obtained the diffusivities of Mg at different temperatures. Figure 6 show the results versus reciprocal temperature and the activation enthalpy obtained for Mg diffusion. These values for the diffusivity are lower by about a factor of three than those obtained from Kirkendall interdiffusion experiments(*46*) but the activation enthalpy is within 10% of that found in those measurements. Over the time

scale of our experiments the mean velocity of the solid/electrolyte interface is of order 10^{-9} cm s^{-1}, but our simple analysis assumes uniform recession of the solid/liquid interface and must therefore underestimate the growth rate of the negative dendrites by an amount that will scale with the volume fraction of porosity within the negative dendrite zone.

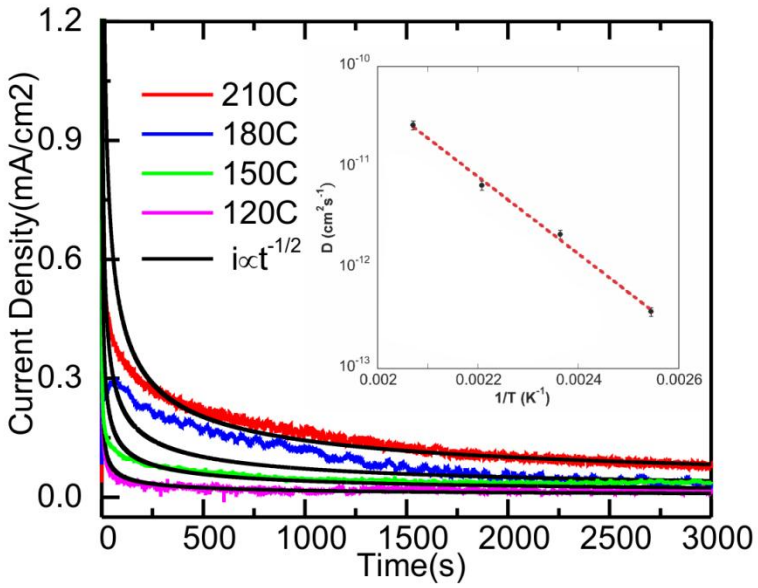

Figure 2.8 Current decay curves for dealloying of $Mg_{0.10}Cd_{0.90}$ at different temperatures, with fitted lines in black. The inset is as-interpolated curve of Mg chemical diffusion coefficient vs. reciprocal temperature

2.4.2 Kirkendall voiding during interdiffusion in Mg-Cd

Chemical diffusion in an alloy with different elements at different rates tends to accumulate vacancies at the faster diffuser side, which is the case for our $Mg_{0.10}Cd_{0.90}$ dealloying. As described in the introduction, this system has been examined with regard to the Kirkendall effect(*46*); however this early work apparently did not examine the

resultant microstructure for voiding. It showed that Mg atoms diffuse ~2 – 3 times faster than Cd at 210 C implying that vacancies and voids will tend to accumulate on the Mg-rich side of a diffusion couple. In principle, a similar process should be occurring during solid-state mass transport controlled dealloying, but the shape of these voids and their location should be distinct from the negative dendrites described above. In an ancillary Kirkendall voiding experiment, a 500 nm thick layer of Cd, mimicking a dealloyed Cd-rich layer, was electrodeposited on to an electropolished $Mg_{0.10}Cd_{0.90}$ alloy surface. Figure 2.9 is a FIB-milled cross-section showing that the resultant microstructure contains nanometer-size isolated voids that mainly accumulate on the $Mg_{0.10}Cd_{0.90}$ alloy side of the interface. It is notable that the voids evolved to depths (as measured from the interface of the diffusion couple) significantly deeper than the penetration depth of the negative dendrites in dealloyed samples.

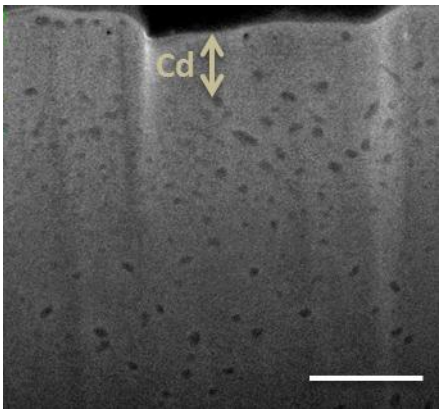

Figure 2.9 Cross-section view of the bilayer sample annealed in the Kirkendall voiding experiment. The scale bar is 1 um

2.5 Conclusions and remarks

As conclusions for this chapter, in Mg-Cd alloy system, we've shown that under percolation threshold of the less noble element, dealloying could proceed by bulk

diffusion when its rate is sufficiently high, and negative dendrite voids instead of bi-continuous structure will evolve correspondingly and the dendrites have preferred growth direction due to surface energy anisotropy. Additionally Kirkendall voids will form at the condition of negative dendrite formation.

The same scenario can happen for other low melting point alloys and even high melting point alloys for small enough particles, owing to Gibbs-Thompson melting point depression. Another relevant observation exists in $LiFePO_4$ cathode. One report shows "porosity" formation in chemically de-lithiated $LiFePO_4$(*54*). Though the one-dimensional diffusion of Li ions is not in favor of correlating the process to dealloying, a more detailed examination of the morphology may help to resolve the long debate over the Li transport mechanism in this material.

3 DEALLOYING IN LI ALLOYS

3.1 Background

Among all low melting point alloys, the most interesting and important systems are those being considered in advanced electrochemical energy storage systems such as future lithium-ion batteries, including Li-Si and Li-Sn, et al. Despite the numerous electrochemical and computational studies connected to battery development aimed at understanding the thermodynamics and mass transport of Li in high mobility host reservoirs, we are surprised to find out that only a few of these have specifically addressed dealloyed (de-lithiated) morphologies(*55*, *56*). Most of the commentary related to porosity evolution is vague and often confused with cracking and fracture issues that can occur in anode reservoirs owing to the large volume expansions these systems undergo during lithiation. There are only several reports in the literature linking porosity evolution in these systems to dealloying and none of these discuss bi-continuous morphologies(*57*, *58*).

As we now attempt to introduce dealloying theory to Li alloys, the focus is mainly divided into two parts. Unlike Mg-Cd, the dramatic differences between the components with respect to atom size, crystal structure and bonding cast doubt on whether the dealloying theory can be fully applied to Li alloys. We will first access the process by aqueous free corrosion dealloying, and then examine factors affecting morphology evolution electrochemically. The second part will on the bulk diffusion's effect on dealloying morphology, tested by varying dealloying rate.

3.2 Experiments

In aqueous chemical de-lithiation experiments, Li / metal bi-layer samples were prepared by heating a Li sheet and a metal sheet under external pressure at 100C for 3 hours, all inside the UHP Ar purged glovebox. The samples were then completely de-lithiated in a water / acetonitrile (Sigma Aldrich) mixture (1:1 v/v) within about 10 mins.

Sn particle electrodes were made by binding commercially available particles to copper foils. 100 mesh (Alfa Aesar), 1~5 um (Sigma Aldrich) and ~100 nm (Alfa Aesar) Sn particles were respectively mixed with Super-C45 carbon black (TIMCAL) and Polyvinylidene fluoride (Sigma Aldrich) in 5:3:2 weight ratios in N-Methyl-2-pyrrolidone (Sigma Aldrich). The as-mixed slurry was pasted onto a copper substrate with a thickness between 10~15um (one monolayer of particles), and dried under N_2 at 60C, to maintain the size, shape and particle separation. The Sn electrode (a current collector was beneath for Sn sheets), polymer separator, counter electrode Li sheet (Sigma Aldrich) and Cu current collector were assembled in sequence and sealed inside a pouch cell, under Ar protection; 1M $LiPF_6$ in ethylene carbonate / diethylcarbonate (1:1 v/v) (Novolyte), in which the separator was soaked, was used as the electrolyte. All the polarization experiments were carried out in a three-electrode cell of similar configuration, with consistent work electrode surface area (Sn mass), and an additional Li sheet as the reference electrode.

Electrochemical experiments were all performed in Gamry series-G potentio-stats. Potentiostatic lithiation were done by holding at various low voltages for 10000 seconds (50ks for Sn sheet and 100 mesh particles); the electrodes were then discharged at 1V vs. Li^+/Li till the current dropped down to about 10mA/g. As for galvanic experiments (C/n),

the total charge was obtained by charging a testing cell of the same electrode surface area within voltage range between 2.5V (1V for capacity fading test) and 0.05V, and the average total charge was between 890-936 mAh/g (993mAh/g as the theoretical value). For a C/1 discharging experiment, the current applied was 993mA/g, corresponding to about 20 $\mu A/cm^2$ assuming average 2 μm diameter particles with 200% volume expansion. We also found charging methods (potentiostatic or galvanostatic) had no impact on the morphology. Polarization curves were obtained right after a C/2 charging.

To uncover the electrode morphologies, Sn electrodes were taken out the cell and kept in acetonitrile for overnight to wash off the solid/electrolyte interphase (SEI) layer.

3.2 Aqueous dealloying of Li alloys and bi-continuous structure formation

As an initial assessment of the morphology from delithiation, Li-Sn, Li-Pb, Li-Cd, and Li-Bi alloys (bi-layer samples) were dealloyed by free corrosion in aqueous solution. The nanoporous structure shown in Figure 3.1 is the typical morphology obtained via dealloying. Due to the alloy preparation method, the composition of the alloys would not be uniform, which yielded a wide distribution of ligament sizes, most apparent in the case of Sn. Nevertheless, the average ligament sizes for all metals are considerable larger than those of dealloyed noble metal alloys, because of the faster surface diffusion. The correlation between the steady state ligament size controlled by surface diffusion and intrinsic metal property will be discussed in more details in Chapter 4.

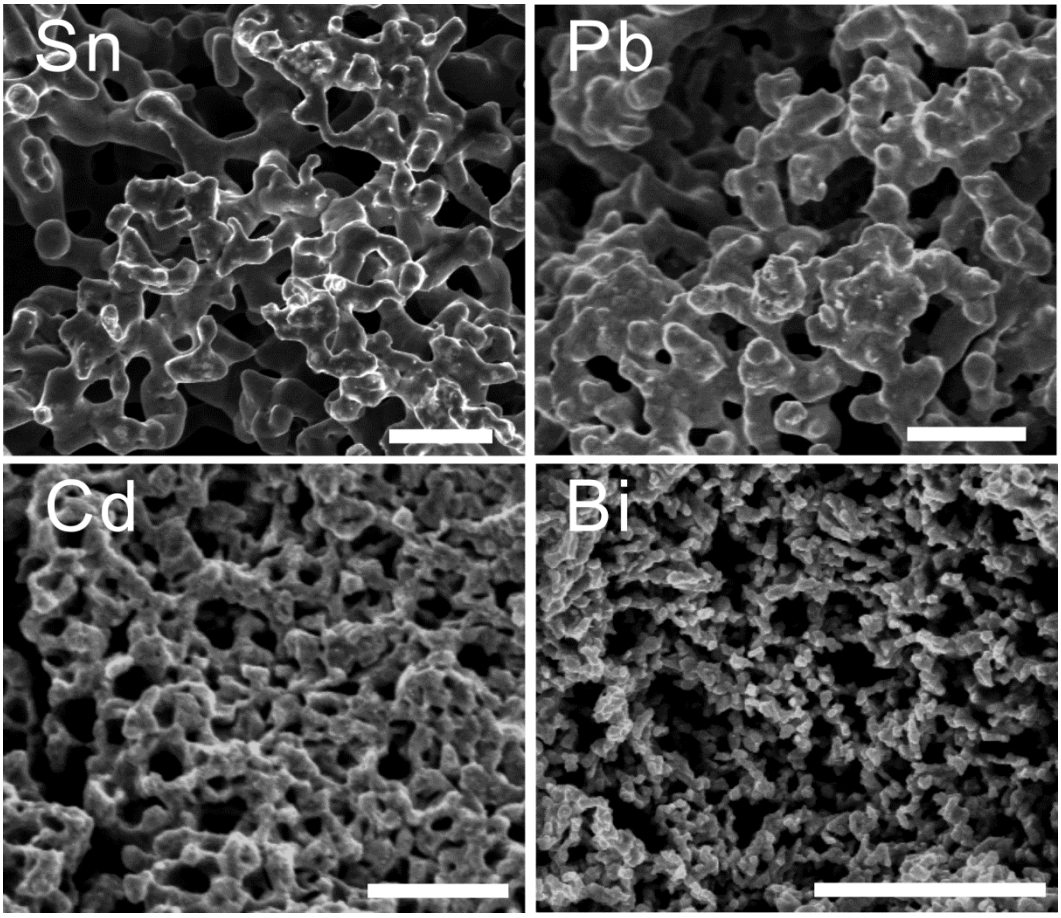

Figure 3.1 Bi-continuous nanoporous morphologies resulting from free corrosion de-lithiation of Sn, Pb, Cd and Bi reservoirs in an aqueous electrolyte. The scale bars in the images are 2 μm.

3.3 Composition dependent morphology in dealloying Li-Sn alloy

In order to understand the factors controlling morphology evolution in these systems, we chose to focus on Li-Sn alloy as it is still a popular candidate for high capacity lithium ion anodes and abundant data is available from extensive research on the system.

Alloying, or as described herein, lithiation, was performed at various potentials to obtain well defined compositions of Li-Sn alloy in particulate Sn electrodes. The alloys were then dealloyed at 1V vs. Li^+/Li.

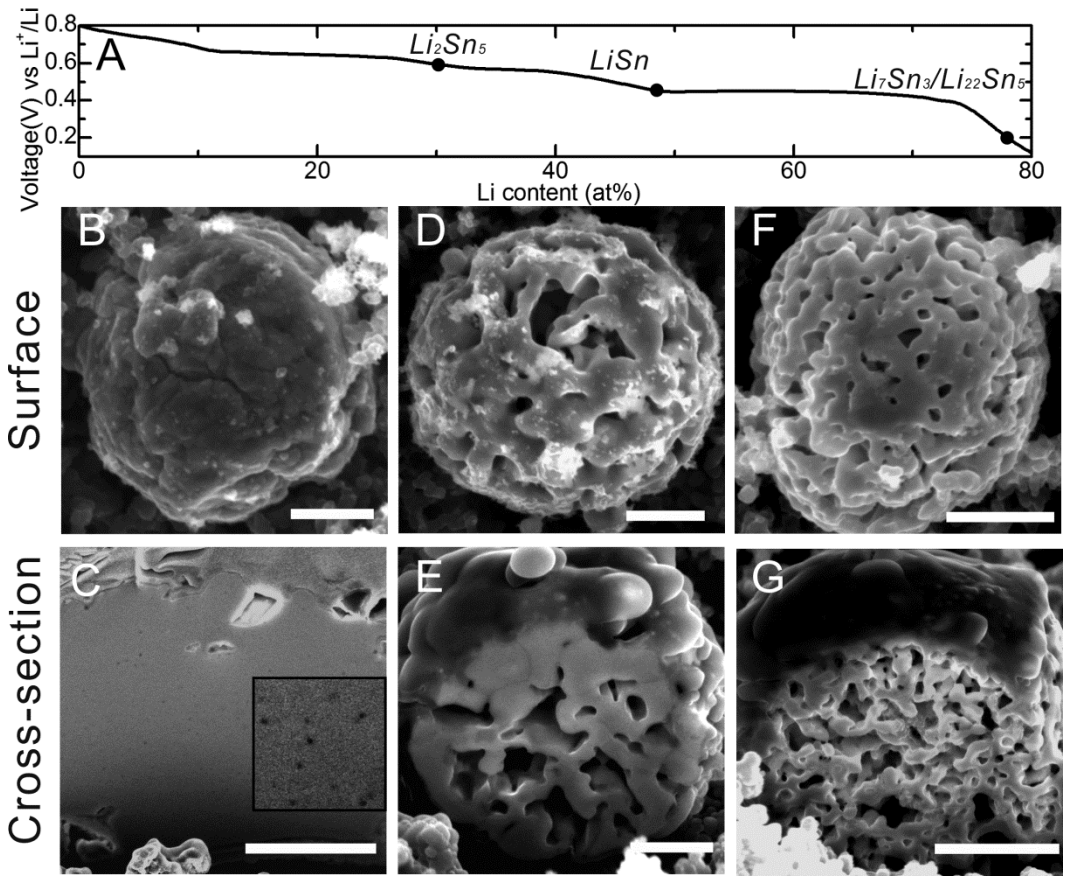

Figure 3.2 (A) voltage-composition curve for Li-Sn modified from a C/20 charging curve. SEM images and FIB cross-sections of (B, C) $Li_{0.30}Sn_{0.70}$, the inset is the magnified cross-section by 2 times; (D, E) $Li_{0.48}Sn_{0.52}$; (F, G) $Li_{0.77}Sn_{0.23}$. The scale bars are 500nm.

As shown in Figure 3.2, Sn particles containing 30 at% Li or less showed no evidence of bi-continuous porosity formation, which can be viewed as the parting limit of this system. While the dealloying was carried by bulk diffusion, the absence of negative dendrite structure as seen in dealloying $Mg_{0.10}Cd_{0.90}$ is most possibly due to grain boundary formation, which will be discussed in session 3.6. On the other hand, Kirkendall voids which were convoluted with negative dendrite in the case of $Mg_{0.10}Cd_{0.90}$ are now apparent.

At concentrations of order 50 at% Li, porosity is evident. Additionally, close inspection of Figure 3.2E shows that the dealloyed particle has a partial hollow-core structure that developed owing to plastic collapse of ligaments where new grain boundaries are also present. This type of structural evolution has been seen before in NPG annealed at the same homologous temperature as room temperature for Sn (see session 4.2.3 for further discussion). Figure 3.2G shows that for Li concentrations larger than ~ 70 at% a bi-continuous morphology similar to that in NPG evolves. The difference in the ligament/pore size apparent by comparison of Figure 3.2E and G is a result of the difference in starting composition of the alloy, which has been seen in case of Ag-Au alloy dealloying.

3.4 Particle size dependent morphology in Li-Sn alloy

There are also effects on the dealloyed morphology connected to the physical size of the reservoir. Figure 3.3 shows how sample size alters morphology under otherwise identical conditions. For Sn particles of order 2um in diameter originally containing ~70at% Li, dealloying yields a ligament size of order 100 nm but for particles of diameter less than ~ 300 nm porous morphologies do not evolve. This is in analogy to behaviors observed on dealloying of noble metal alloy nanoparticles. That is, for particle diameters less than ~2-3 times the ligament size dealloying does not produce bi-continuous morphologies.

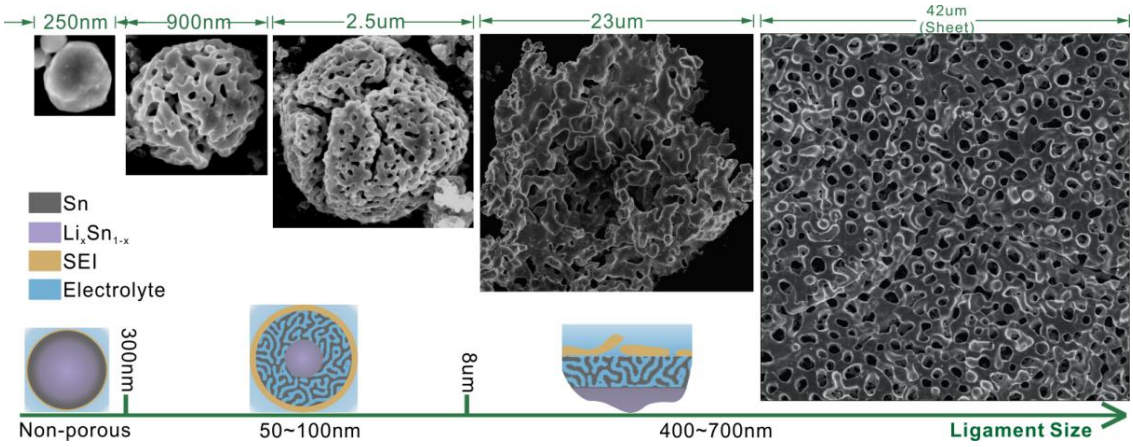

Figure 3.3 The effect of particle size on dealloyed morphologies

Figure 3.3 also shows that as the reservoir size increases the length scale in the porous structure increases. For large particles and planar Sn sheets the porous length scale is ~ 500-700 nm which is similar to that shown in Figure 3.1. We believe that this difference in length scale is related to the stability of the SEI layer, as illustrated in Figure 3.4. This layer has the effect of reducing the coarsening rate of the porous structure by reducing the rate of surface diffusion. During lithiation there is about a 260% increase in the reservoir volume(*59*) independent of reservoir size. However, the displacement associated with this volume change scales with the reservoir size resulting in a larger degree of SEI layer deformation and corresponding mechanical destabilization of this layer. This tends to reduce the effect of the SEI layer on coarsening. The reason why the small ligaments were stable against in-air coarsening after SEI was dissolved is believed to be the oxide layer formed during the dissolution SEI in the acetonitrile. The interpretation was also confirmed when we utilized it to fabricate a bi-modal nanoporous Sn sheet. The sample was prepared by two cycles of potentiostatic charging/discharging, first at 0.4V/1V and second at 0.2V/1V. In Figure 3.4, the larger level porosity contains ligaments of 1um size,

and the smaller level porosity is around 100nm, which was stable against coarsening since the new SEI formed in the second cycle remained conformal on the ligaments.

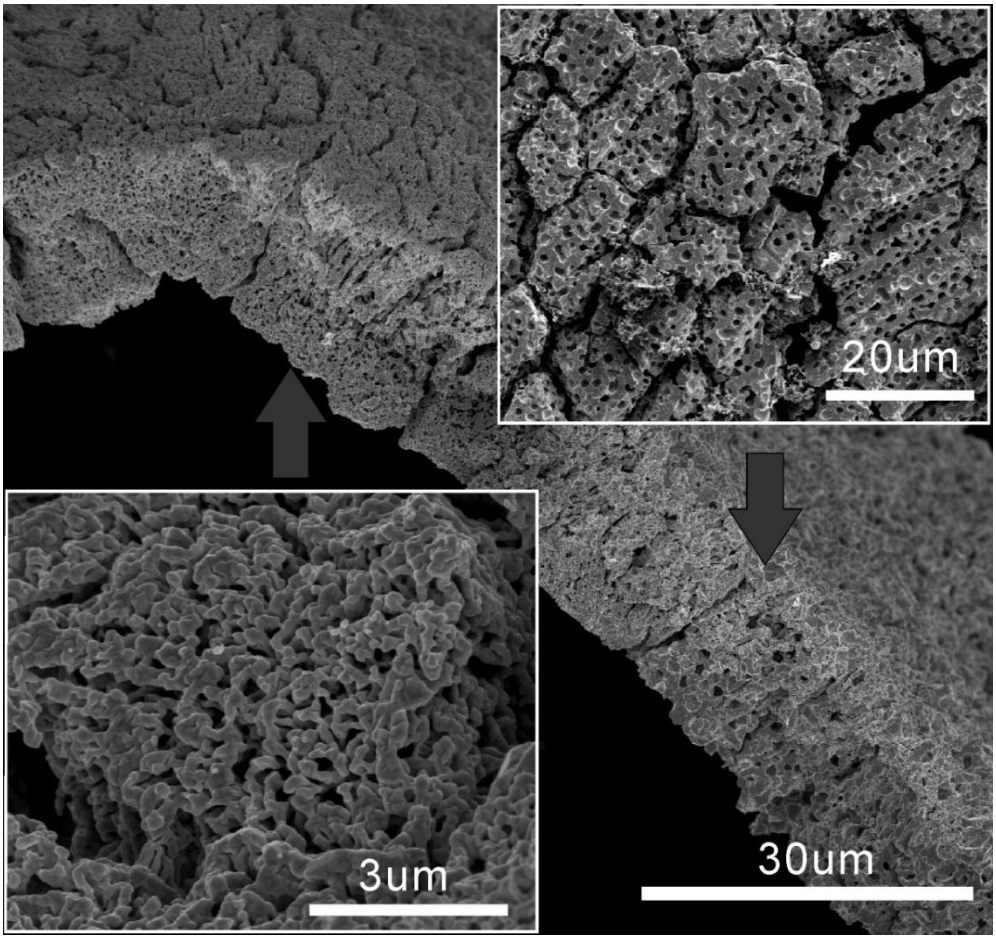

Figure 3.4 Bi-modal porous Sn sheet obtained after two potentiostatic cycles

3.5 Dealloying rate dependent morphology in Li-Sn alloy

Dealloying rate effect was studied by discharging Sn particles at various C rates (Figure 3.5A and B). The effect of de-lithiation rate on morphology evolution in Li-Sn is shown in Figure 3.6A~D. At a discharge rate of 10C and 1C, the bi-continuous length scale is similar to potentiostatic discharging and for a C/2 rate this length scale increases to about 200 nm. At a C/10 discharge rate the dealloyed particle morphology is not bi-

continuous, which is interpreted as a case of passivation by surface diffusion. When alloys with minuscule lattice diffusion are dealloyed at too low a current density compared to the surface diffusion rate, that is, below critical potential, a compact layer of the more-noble element forms that results in a passivation-like process that quenches dealloying; in low melting point alloys like Li-Sn, the low dealloying rate maintains via bulk diffusion through the Sn rich layer.

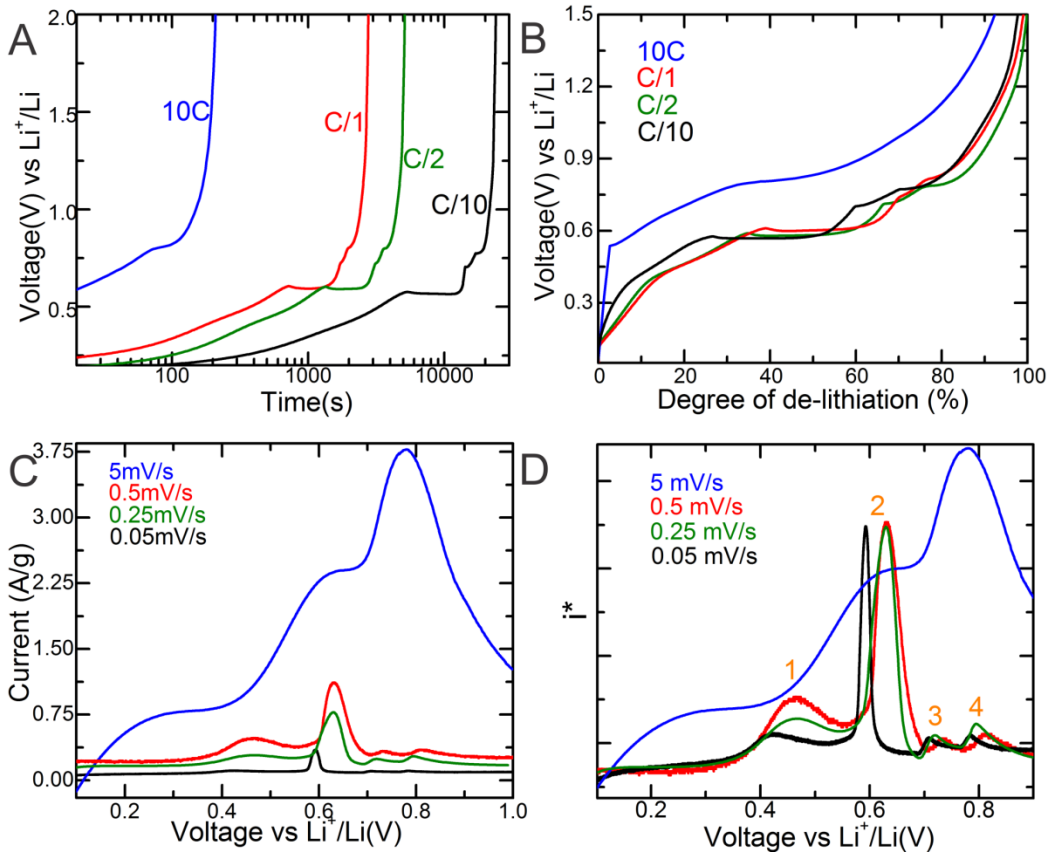

Figure 3.5 (A, B) chronopotentiometry curves and (C, D) polarization curves without and with normalization, respectively

The chronopotentiometry data for the C, C/2 and C/10 discharges demonstrates that the voltage profiles are nearly identical, indicating that at equivalent remaining Li contents the alloy surface compositions were similar despite the differences in

morphology. We conclude that at these discharge rates solid-state diffusion is sufficient to compositionally homogenize the particles during dealloying. In order to investigate how this happens, we examined the dealloying polarization curve behavior at different sweep rates and scaled the current by the square root of the sweep rate. For mass-transport limited de-lithiation, the scaled wave peak heights should be independent of the sweep rate(*60*). Figure 3.5C shows this data for sweep rates of 5.0, 0.50, 0.25, 0.05 mVs^{-1}. The waves in the polarization curves correspond to de-lithiation of Li-Sn phases initially present and evolving on the electrode surface during potential scanning. These sweep rates result in de-lithiation times approximately equivalent to discharge rates of 10C, C, C/2 and C/10 respectively for which bi-continuous morphologies evolve for all but the lowest sweep or discharge rate. Except at the highest sweep rate, we observe scaling of the wave heights of all the waves except for that labeled 1. Since a bi-continuous morphology cannot evolve under conditions of solid-state mass-transport limited dealloying, we associate porosity formation at the 0.50 and 0.25 mVs^{-1} sweep rates with this wave. This conclusion is confirmed by results of potentiostatic de-lithiation experiments that demonstrate the formation of a bi-continuous nanostructure at 0.5 V (Figure 3.6E). The second large wave labeled 2 in the polarization curves is associated with de-lithiation of the ligaments comprising the bi-continuous morphology that evolved during the first wave. There is no second level of porosity that forms within the ligaments owing to the size effect previously discussed. For the 5 mVs^{-1} sweep rate these waves become convoluted and good sweep rate scaling of the peak heights is no longer apparent indicating that the bi-continuous morphology is evolving throughout the entire polarization curve.

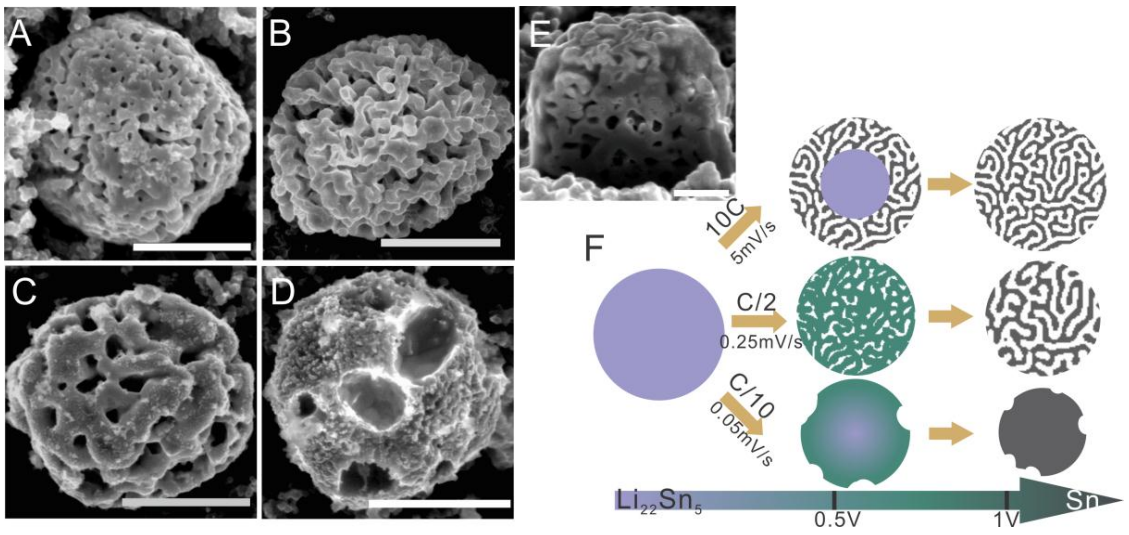

Figure 3.6 (A~D) Sn particles dealloyed at rates of 10C, C/1, C/2 and C/10 respectively; (E) particle dealloyed at fixed potential of 0.5V; (F) cartoons illustrate the morphology evolution at different rates, with the coloring for different alloy compositions.

3.6 Grain boundary formation during lithiation / de-lithiation

In a few of the above images (e.g. Fig. 3.3 and Fig. 3.6D), there are large numbers of grain boundaries present which were absent in the initial Sn substrates (Fig. 3.7 as examples). It's not surprising since in the case of silicon, lithiation could completely destroy the crystallinity of the solid. We believe this process is more likely to happen during lithiation as the huge volume increase may impose a large stress to drive grain growth. The biggest effect from the grain boundary formation to the morphology evolution is the negation of the void dendrites during lattice diffusion supported dealloying, even at high dealloying potential (Fig. 3.7b). The grain boundaries will serve as shortcuts to lattice diffusion and thus consume the vacancies generated by de-lithiation.

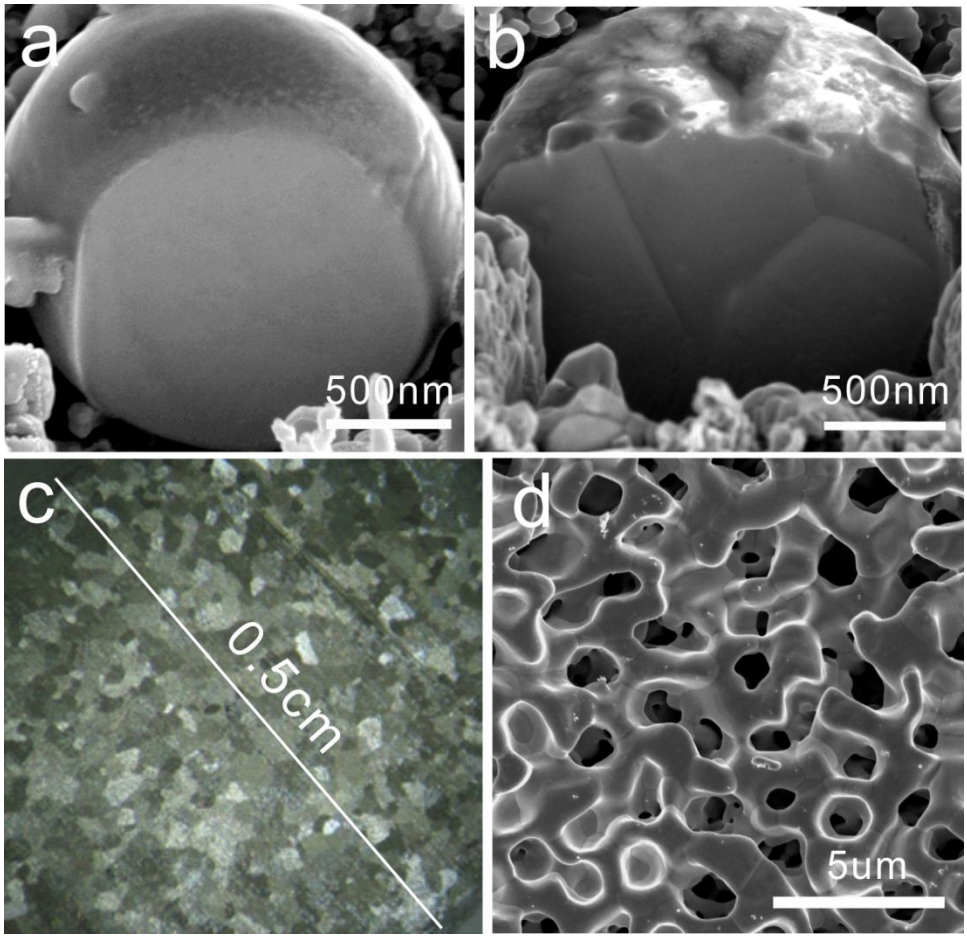

Figure 3.7 Grain size comparisons between virgin Sn substrates and Sn after lithiation / de-lithiation circle for (a, b) Sn particles, and (c, d) Sn sheets. The particle in (b) was lithiated to 0.6V and de-lithiated at 2.5V, and the sheet in (d) was lithiated at 0.2V and de-lithiated at 1V

3.7 Improving Sn anode cycle stability by nanoporous structure

The nanoporous structure preparation method here can be adopted towards various applications. In particular, it has a potential to improve the lithium anode capacity and performance, for all the merits it inherited from the fabrication method. For instance, we measured in Figure 3.2 the volume change retention from porosity formation. Particles could retain close to half the volume expansion in the fully charged state, which may greatly improve its mechanical stability. At the same time, due to its continuous nature,

the nanoporous can negate binding materials and even current collector if applied to a sheet form, and this will help to achieve higher volumetric and gravimetric energy densities. The way we used to obtain the nanostructure is also facile and more cost-effective compared to methods employed nowadays to improve the anode performance.

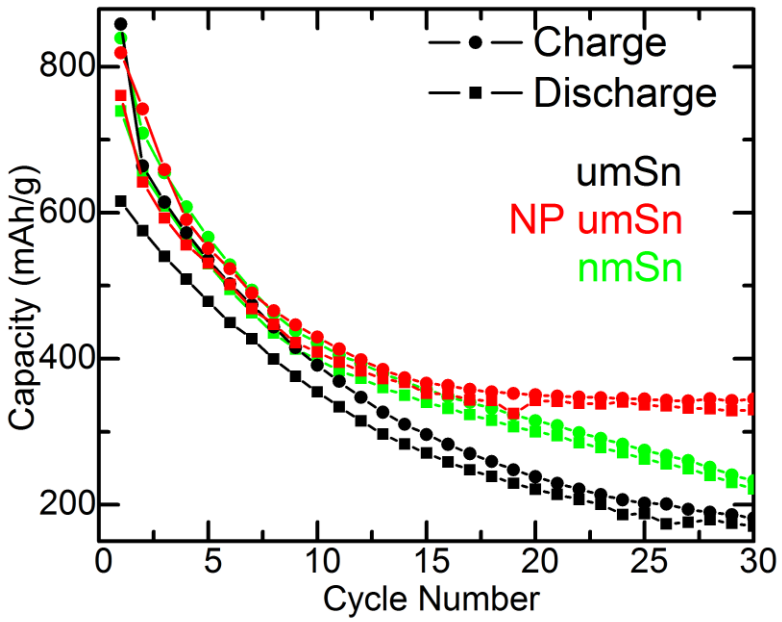

Figure 3.8 Capacity retention tests for different Sn particle electrodes

We made an initial attempt to demonstrate the benefit of the in-situ prepared nanoporous structure by examining particulate Sn electrodes. Here umSn, NP umSn and nmSn separately stand for electrodes containing 1~5um diameter Sn particles, 1~5um diameter nanoporous Sn particles and 100nm diameter Sn particles. The NP umSn electrode was obtained from umSn by potentiostatically charging and discharging it at 0.2V and 0.8V respectively. The tests were carried at rate of C/2, with voltage cut-off between 1V and 0.05V. Figure 3.8 shows there is a significant improvement from

nanoporous Sn particle. The capacities of both umSn and nmSn faded gradually to as low as 200 mAh/g after 30 cycles, similar to previous reports. As for NP umSn, the retention slowed down after 20 cycles, and stayed above 1/3 of the theoretical capacity until the end of the test. Although this value is far from practical satisfactory, it approached the better values reported for pure Sn(*61*, *62*). In addition, no attempt was made to optimize the electrode configuration from the one designed for morphology study, therefore we believe this facile in-situ method can be applied to further improve the alloy based Li anode's performance.

3.7 Conclusions

We show for the first time how well dealloying theory can be applied to Li alloy systems. The bi-continuous porous structure is obtained for various low melting point alloys, and in Li-Sn, the morphology evolution depends on alloy composition and particle size and dealloying rate. Bulk diffusion supported dealloying occurred when surface diffusion outcompetes dissolution rate; it did not produce negative dendrite structure due to grain boundary formation and/or surface diffusion.

4 DEALLOYING THEORY: REVISITED

In previous two chapters, we successfully incorporated the solid-state mass transport process into the dealloying theory by studying Mg-Cd and Li alloys. In addition, the studies extend important factors to unexplored regions, which include surface diffusivity, crystal structure and composition. We also expect our work to stimulate new studies to apply dealloying methods to applications such as solid-state energy storages. All of the above call for a comprehensive review of dealloying theory, which unfortunately does not exist. In this chapter we will attempt to fill this vacancy with a brief summary of the central issues of dealloying, as well as to offer interpretations that apply to all dealloying processes.

As there have been very good reviews on mechanical properties(*63*) and catalysis applications for dealloyed nanoporous metals(*24*), the chapter will be centered around other fundamental aspects. The first part is on the electrochemical responses during dealloying, with a special emphasis on their critical behaviors, and the second half is about the details of morphology evolved during dealloying and coarsening.

4.1 Critical behaviors in dealloying

"Critical" is defined by Merriam-Webster as, relating to or being a state in which some quality, property, or phenomenon suffers a definite change. In dealloying, the "change" can be phrased as following: the start of a sustained selective dissolution process and a concomitant bi-continuous morphology evolution from a macroscopically flat surface. Criticality in dealloying derives from percolation, but it is heavily affected by kinetics (e.g. surface diffusion) which obscures the underlying physical connection to

critical phenomena in the strict sense. Therefore our discussion on "criticality" here should be viewed as "critical-like" behaviors.

The word "critical" really only appears with respect to a dealloying "turn-on" potential or critical potential and this is mainly for historical reasons connected to literature in corrosion. Nevertheless, I believe the concept is applicable to other phenomena in dealloying, which includes parting limit and critical alloy size for porosity evolution.

4.1.1 Passivation

In a binary alloy A_pB_{1-p}, the electrochemical redox potential of A can be obtained from the Nernst equation

$$E = E_0 - \frac{RT}{nF} ln(\frac{a_A}{a_{A^{n+}}}) \qquad 4\text{-}1$$

E_0 is the standard potential of A, R is the gas constant, T is the temperature in K, n is the charge transfer number associated with A redox, and a_A and $a_{A^{n+}}$ are the activities of A in the alloy and electrolyte respectively. Whenever the voltage is higher than that in Equation 4-1, the inability of sustained dissolution of A component should be termed as passivation. In certain electrolytic condition, a pure metal can also passivate (e.g. forming oxides), but in dealloying, the passivation comes from the more noble component. Its effect can be visualized as layers of B atoms on top of the alloy, either forming a near complete coverage to isolate electrolyte (under parting limit)(*64*, *65*), or leaving pinholes that are so tiny that extra energy needs to be paid to forward the dealloying (below critical potential)(*14*, *22*). The passivation persists as assuming no solid-state atomic movement, and a full coverage conformal layer of the more-noble component. These two

properties of the passivation layer give the dealloying sharp turn-on instead of gradual transition, which is exhibited as criticality.

Percolation theory provides a lower compositional bound of this behavior by assuming a stationary interface during porosity formation; in real systems, surface diffusion elevates the critical point because of the tendency of smoothening surface fluctuations. Either with or without surface diffusion, dealloying will still proceed for a limited depth prior to passivation(*14*), as long as applied potential is larger than that predicted by Equation 4-1. This is termed as surface dealloying, which can be significant in small sample size electrodes.

When the lattice diffusion rate becomes significant compared to the dissolution rate, passivation as such no longer occurs. The less noble component rich surface layer will be quickly homogenized and this process continues as dealloying proceeds. Therefore, the cases previously categorized as passivation are turned into bulk diffusion controlled dealloying, and sharp transitions do not exist.

4.1.2 Parting limit

The parting limit is the compositional threshold of the less noble component below which dealloying cannot proceed without the support of solid-state mass transport. The name comes from the macroscopic separation or “parting” of gold from alloys like Ag-Au and Cu-Au. In those two systems, the thresholds are around 55 at% of the less noble component, while for other alloys such as Al-Cu and Zn-Cu the numbers seem to be closer to the percolation threshold 20%. In previous chapters, the morphology

examinations give ranges for parting limits in Mg-Cd and Li-Sn, and all the above numbers are listed in Table 4.1.

Table 4.1 Parting limits for various alloys

Alloy System	Parting Limit (at%)	References
Ag-Au	55	(*4*)
Cu-Au	50~60	(*3*)
Zn-Cu	17~20	(*6*)
Al-Cu	11~16	(*6*)
Mg-Cd	15~45	Chapter 2
Li-Sn	30~48	Chapter 3

As discussed earlier, the lowest less noble metal content for bulk dealloying should be set by the percolation threshold, which is about 20~30 at% for cubic and hexagonal crystal structures. This number can be altered depending on ordering, composition inhomogeneity and atomic size difference. However, the biggest deviation is in the most ideal system Ag-Au in the sense that none of the above factors is heavily involved. The cause has been under debate for a long time, and a recent work by Artymowicz et al.(*33*) revisited the concept of high density percolation proposed in 1988 by Sieradzki et al.(*19*). High density percolation refers to a percolation process where each of the Ag atoms that are in the percolation backbone have at least m near-neighbors that are also Ag. Artymowicz et al. evaluated all the high density thresholds relevant to fcc lattices ($2 \leq m \leq 12$) and compared them to the experimental parting limit of Ag-Au. The found that the threshold for m=9 compared nicely to the experimental result. At concentration lower than 55at% Ag, even though the Ag atoms percolate, the free volume created by cluster dissolution isn't large enough to allow for ion solvation.

We also note that all the measurements of parting limits except that of Ag-Au have been "outdated" because the definitions of critical behaviors described in session 4.1.1 were never followed during the measurements. Thus new examinations will be necessary to complete the discussion.

4.1.2 Critical potential

For dealloying, the critical potential is one of the most studied features initially for its benefit to corrosion resistance. The value of critical potential increases with decreasing less noble component content (until the parting limit), and differs among alloy systems. Unfortunately, a comprehensive set of values only exist for Ag-Au(*4*).

The origin of critical potential is most successfully explained in the framework of percolation theory. In an ideal solid solution A_pB_{1-p}, the average cluster size ξ for the less noble A component can be estimated as(*21*)

$$\xi = a\frac{1+p}{1-p} \qquad 4\text{-}2$$

where a is the nearest neighbor spacing. The size marks the initial diameter of the pits at the dealloying front, which adds a Gibbs-Thompson free energy term of $\frac{4\gamma V_m}{\xi}$. Combined with Equation 4-1, we can reach to the expression of critical potential as

$$\mathrm{E} = \mathrm{E}_0 - \frac{RT}{nF} l\mathrm{n}\left(\frac{\mathrm{a_A}}{\mathrm{a_{An+}}}\right) + \frac{4\gamma V_m}{nF\xi} \qquad 4\text{-}3$$

Here again, γ is the interface energy and V_m is the molar volume of the alloy. In addition, a kinetic term associated with surface diffusion will be present to further elevate the critical potential(*4*). Equation 4-3 gives accurate predictions on the critical potential

differences among vary alloy compositions, proved by the work in Ag-Au as well as multilayer Ag/Au samples with manipulated "cluster" sizes(*22*).

Besides alloy composition, there are other factors significantly affecting the critical potential. For alloys all containing 75at% less noble component, Cu-Pt and disordered Cu-Au show ~100mV higher critical potentials than Ag-Au. This difference is believed to be from the bonding energy, i.e. the a_A term in Equation 4-3. The critical potential of ordered Cu_3Au alloy was measured to be 250 mV higher than disordered $Cu_{0.75}Au_{0.25}$, which cannot be fully covered by the ordering energy; instead, if the cluster size is calculated by the thickest stacking Cu layers in the ordered crystal structure, rather than the random percolating cluster, the difference can be well explained.

Finally, we discuss effects from significant lattice diffusion. The critical potential should still be quite distinguishable because it separate two types of current-voltage behavior — below the critical potential current density quickly goes independent of voltage into mass-transport control (decays with $t^{1/2}$) and above the potential it turns to Bulter-Volmer type behavior. However, the measurement of the critical potential will be significantly altered. As for alloys without solid state mass transport, both polarization and potential-holding have been applied to obtain critical potentials(*4*, *13*). But polarizing a low melting point alloy will result in a passivation layer that might increase the critical potential or even suppress the bi-continuous structure evolution as in the C/10 dealloying of Li-Sn alloy. Therefore, critical potential measurement can only be performed by potential-holding when bulk diffusivity is high.

4.1.3 Critical electrode size

As shown earlier in 3.4, there exists a size threshold below which bi-continuous porous structure does not evolve. Compositional analysis shows that dealloying of noble-metal particles below the size threshold results in noble-metal shell and alloy core retaining parent alloy content, corresponding a passive state(*27*, *66*). So the critical electrode size is both electrochemically and morphologically a similar concept to the critical potential and the critical composition (parting limit).

The cause of the critical size is yet to be explored. We discuss two speculations as follow. The first is that the appearance of the critical size is due to the increase of surface diffusivity, because smaller size particles tend to generate more defect sites (step and kink) on the surface which facilitate the adatom movement. However, one derivation from this speculation is that ligament size should increase with decreasing particle size, which is never observed. Moreover, in the case of Sn particles, the critical size (~300nm) is too large to differ significantly from bulk alloy with respect to defect sites. The second speculation is drawn in Fig. 4.1. Fluctuations develop at the initial stage of dealloying. By assuming the surface diffusion's contribution to passivation is limited to the positive curvature parts of the fluctuations and the dissolution occurs at the valleys, we can approximately define a ratio between their areas. In a potentiostatic dealloying experiment, this number stays constant for a planar alloy whereas it will be decreasing in particles of a size that is not significantly larger than the fluctuation amplitude that natively assume to be related to steady-state ligament size (Fig. 4.1A). This will lead to passivation once dissolution is outcompeted after a shallow dealloying depth.

At the same time, we note that even under the critical size, complete dealloying can occur in cases where potential cycling instead of potential static holding is applied(*67*, *68*). A possible explanation we can offer is that, noble metals such as Pt and Au go through reversible surface oxidation and reduction in the potential region of cycling, and this process tends to induce inter- and intra-layer atomic movements that expose the buried atoms to the electrolyte.

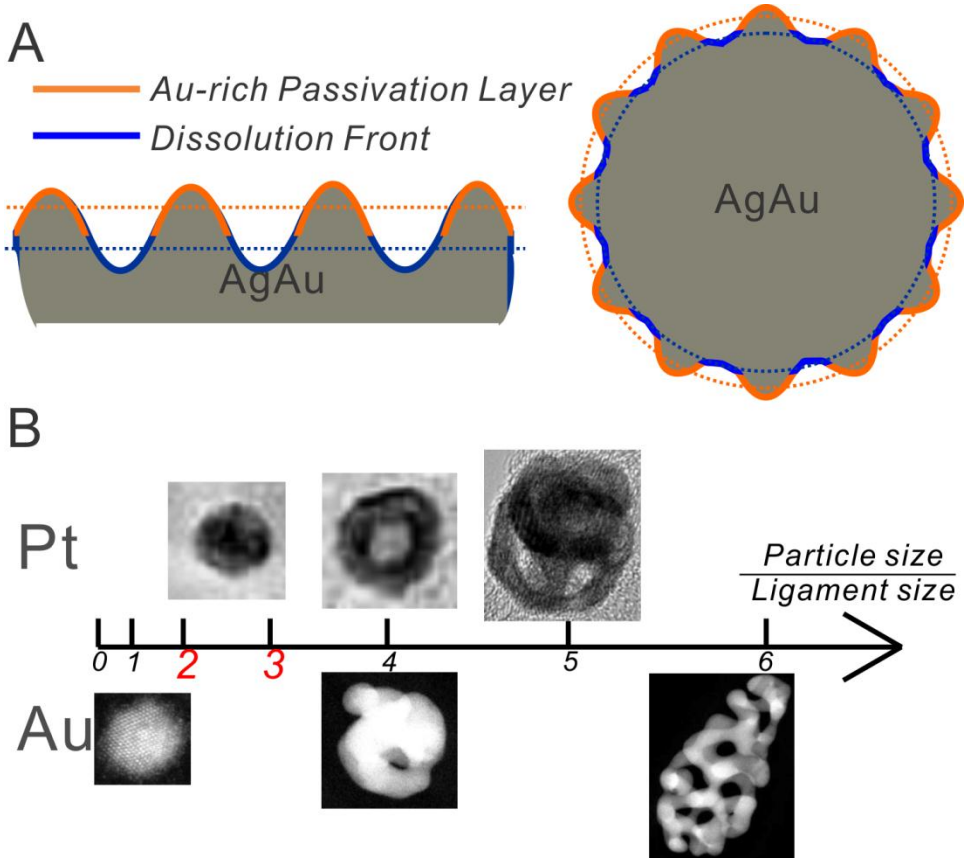

Figure 4.1 (A) cartoon illustrating the difference between planar and particulate alloys, with dotted lines denoting the effective areas for dissolution and surface diffusion, respectively; (B) critical size effects on porosity formation in Pt and Au alloys

4.2 Morphology characteristics

Dealloyed morphology is often equated to the bi-continuous structure. The is true to a degree that most of aspects associated to dealloying will be reflected by the details of the nanoporous structure. The complex combination of these ingredients also acts against an accurate prediction of properties for a specific bi-continuous structure. The discussion here will also be centered on the bi-continuous structure. We will try to rationalize the structural evolution for all dealloying processes.

4.2.1 Theoretical background

Similar as to the critical behaviors, percolation theory provides the basic frame of the bi-continuous structure. In a binary alloy A_pB_{1-p} the cluster size of A in Equation 4-2 limits the smallest pore size one can obtain from dealloying, while the cluster size of B gives the limit for ligament size. However, all the structures seen in the literatures have been reconstructed by surface diffusion, and even if a good care is taken, the nanoporous structure still undergoes rapid coarsening in a short time (*12*).

It's clear why surface diffusion acts to smoothen the nanoporous structure, but the understanding of how it works has not progressed much since Forty's discussion. A rule for rough Au surface smoothening based on Herring's model was directly adopted by Corcoran et al.(*69*), described as

$$r^4 - {r_0}^4 = \frac{2\gamma a^4 D_s t}{\mathrm{kT}} \qquad 4\text{-}4$$

Where r and r_0 are the final and initial ligament sizes respectively, γ is the surface energy, D_s is the surface diffusivity, t is the total coarsening time, k is the Boltzmann constant and T is the temperature. The value of r_0 can be estimated by the mean cluster

size of the noble component from Equation 4-1, and it is often a very small number (~1 nm). Undoubtedly this formulation is a simplified description, as the bi-continuous structure is topologically more complicated than two-dimensional surface roughness. But it predicts rules of porous morphology evolution that have been constantly confirmed, such as the $t^{1/4}$ dependence for coarsening(*70*, *71*). This type of time dependence results in a pseudo steady-state length scale, meaning that after it stabilizes within about one day it takes weeks or longer to double the size(*12*). In the following discussion, steady-state ligament size will be used as the representative length scale, instead of the mean pore size which is harder to be accurately measured.

Another model of coarsening based on solid-state Rayleigh instability was recently introduced by Erlebacher(*34*) to explain a surprising observation of encased voids inside the ligaments(*72*). The Rayleigh instability is also based on energy minimization, and it better describes the pinch-off events of the saddle point configurations that maintain the structure's self-similarity during coarsening. The process can be explicitly explained by looking at a slim cylinder. In Fig. 4.3A, longitudinal fluctuations with different wavelengths will tend to develop at the cylinder surface (interface). Small perturbations quickly die out, but once the wavelength exceeds its circumference, the cylindrical shape will not be stable, because the average radial curvature decrease outbalances the longitudinal curvature increase and the system moves towards a lower energy state. In bi-continuous porous metal, both the ligament and the pore channel can be viewed as cylinders and the surface diffusion provides for the mechanism of the instability during the coarsening.

4.2.2 Length scales in bi-continuous structures

As discussed in the previous session, at ambient temperature the ligament size achieves a pseudo-steady state value after about one day. The parameter used most often to tune this length scale is the surface diffusivity. It depends exponentially on temperature, which makes post-annealing a powerful tool. Starting from ~10 nm, the NPG ligaments can be enlarged to micrometer level by 10 minutes of annealing at 600 C(*12*), and the annealing process follows the $t^{1/4}$ rule, as long as sintering is not involved. The temperature effect can also be applied during dealloying, although less tunable due to the limit of the electrolyte(*70*).

Another way of controlling surface diffusion can be achieved at the electrode / electrolyte interface, often along with dealloying. A slight change of electrolyte composition may greatly affect the nanoporous structure, since the amount of addions required to cover the surface is small compared to the electrolyte volume. The addition of halide ions is the most common way to increase the length scale in-situ(*26, 69, 73*), and passive surface layers have been used to suppress the surface diffusion controlled coarsening. Here the passive layers can be metal oxides(*74*), precipitates(*75*), and even SEI layers as shown in Chapter 3.

Depending on the particular alloy (noble-metal, Li-Sn, Mg-Cd) there is a wide variation in the pseudo-steady state ligament size. We can understand this by consideration of the surface diffusion. There is an empirical correlation that the activation energy of surface diffusion is proportional to the metal's melting point(*76*). A collection of nanoporous metal ligament sizes from literatures (Table 4.2) were plotted together with the porous metals we obtained in Chapter 3 versus their T_H, shown in Figure 4.2.

The fitted line crosses all points surprisingly well. Even those with high bulk diffusivity fit the trend, because all ligament sizes are still far below the point where bulk diffusion takes over the coarsening process from surface diffusion(*77*).

Table 4.2 Data used in Fig. 4.2

Parent Alloy	Ligament Diameter (nm)	Reference
$Ag_{70}Au_{30}$	20±10	(*78*)
$Co_{75}Pt_{25}$	3±1	(*31*)
$Mn_{70}Cu_{30}$	16±4	(*79*)
$Co_{20}Pd_{80}$	6±2	(*80*)
$Al_{77}Ag_{23}$	35±5	(*81*)

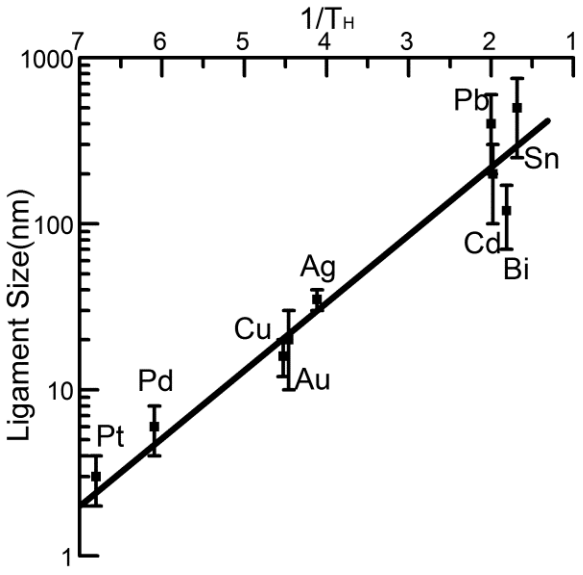

Figure 4.2 Ligament size and homologous temperature correlation for porous metals

4.2.3 Ligament collapsing

During nanoporous metal annealing, one phenomena observed along with ligament coarsening is the collapse of ligaments (*12*, *82*). It's similar to sintering, which annihilates the porosity. The collapse seems occurs at too low a temperature to involve creep, and the bi-continuous structure is robust enough meaning that the self-weight or "body force" of ligaments does not seem to be sufficient to cause this behavior.

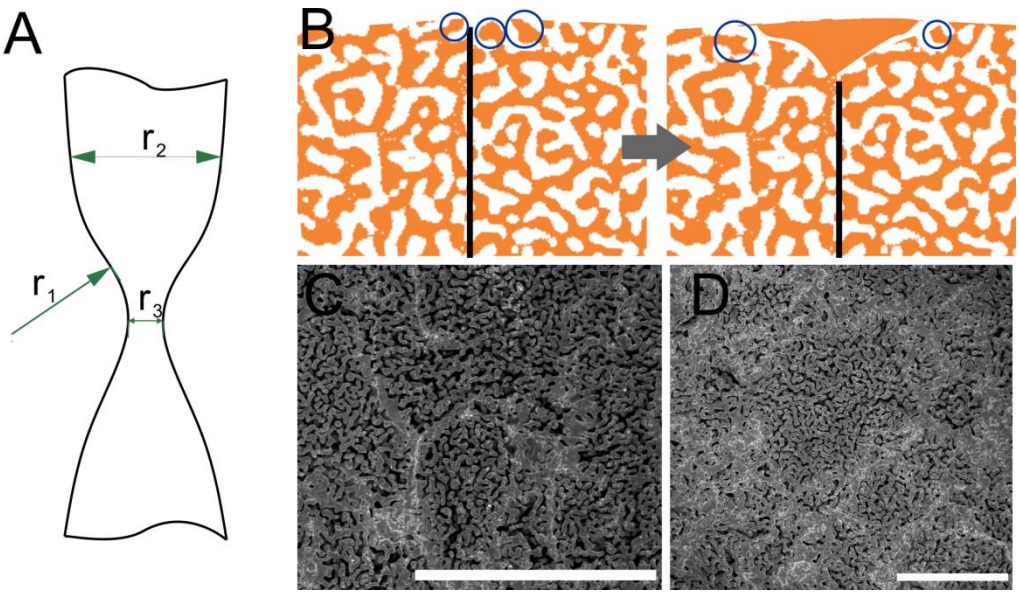

Figure 4.3 (A) Rayleigh instability in porous metals; (B) ligament collapsing mechanism at the grain boundary, with ligaments susceptible to collapsing circled in blue; (C) and (D) NPG with collapsed ligaments after 10 mins and 1 h annealing at 500C, in which the collapsing starts at grain boundaries and grow on the surface. The scale bars are 40um

To understand the mechanism of collapsing, we refer back to the Rayleigh instability. The robustness argument for the porous structure is founded on two assumptions for the ligaments, which are uniform size and high connectivity. The first assumption apparently does not hold as the Rayleigh instability renders radial distribution along ligaments. The same process also decreases the ligaments' connection, which won't by itself result in

any weak points in the bulk because any ligament that loses connections due to pinch-off will be consumed to enlarge others. However, there are specific sites that may behave differently. At the surface, ligaments are under-connected compared to those in the bulk; at the intersection between grain boundary and surface, due to preferential dealloying induced by composition segregation as well as grooving, ligaments with even fewer connections exist, as circled out in Fig. 4.3B. One can describe those ligaments as dangling, borrowing the concept of dangling bond, meaning that they are more likely to suffer structural change. Once a dangling ligament gets pinched-off, it falls off the nanoporous network. The repetition of this event accumulates solid clusters, adjacent to which are more ligaments susceptible to collapsing. The process should occur at any temperature, but at low temperature accumulation of the clusters might be too slow to be observable. At elevated temperature, collapsing starts at the grain boundaries on the surface, and propagates primarily along the surface (Figure 4.3C, D). It may also move downwards into the bulk, when the temperature is high enough to destabilize all the ligaments across the surface.

We note that in a nanoporous particle, when the particle size approaches the ligament size (certainly above the critical size to contain the structure), the ligaments on the surface are further under-connected due to the particle curvature, therefore more susceptible to collapsing and forming a core/shell structure, such as what we saw in Chapter 3.

4.2.4 Volume change

During the dealloying process, the massive atomic rearrangement will result in volume change that can't be neglected. There is only one systematic examination on volume change by Parida et al.(*83*), so to make a comparison we performed measurements on the porous Sn particles in Chapter 3. Solid / void area ratios at the cross-section were used to estimate the volume changes, and initial volumes (alloyed state) were calculated from the theoretical alloy densities. When the bulk diffusion is taking part in the dealloying as in Figure 4.4, significant volume shrinkage occurs since fewer vacancies agglomerate into voids. In the case of active surface diffusion alone, the volume change can be divided into two groups. At fast dealloying rate, such as high overvoltages for Ag-Au(*83*) and the potentiostatic dealloyed Li-Sn, almost half of the volume initially occupied by the less noble metal vanishes, whereas slow-rate-dealloyed Ag-Au retains its size well(*71*, *83*). While Parida et al. speculated a few operating mechanism of the volume change, it is still unclear to us what the controlling process is.

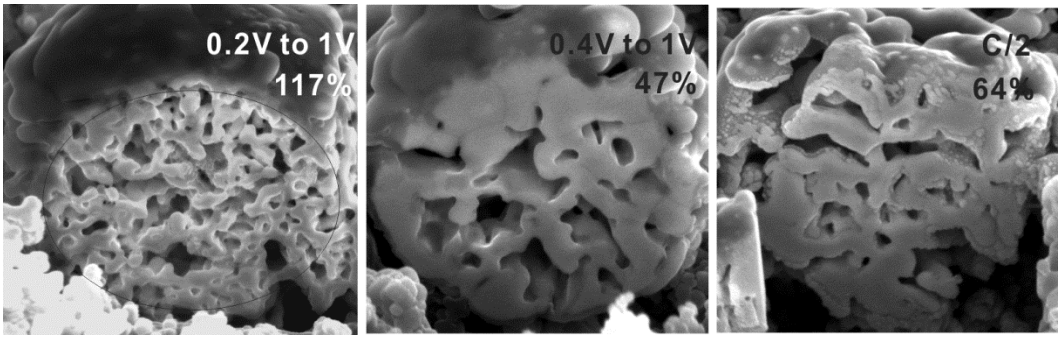

Figure 4.4 Volume change in dealloyed Li-Sn alloys

4.2.5 Encased voids

A surprising feature and interesting feature in NPG is that of isolated encased voids within the ligaments (see Figure 4.5A for example). Rosner et al. reported it for the first time and confirmed their complete encapsulation by tomography(*72*). As mentioned in session 4.2.1, Rayleigh stability was employed to explain its formation (*34*). Because of the symmetry between ligaments and pore channels, the same pinch-off process can occur to a pore channel surrounded by solid metal. The as-formed isolated voids will be morphologically stable since they do not participate in coarsening. In fact, decades ago, similar types of voids formation have been extensively studied and explained by Rayleigh instability for metal and ceramic grain coarsening(*84, 85*).

The interpretation is just the start of an interesting scenario. During the encasing process, the electrolyte may remain in the encased pore. The encased voids should not be vacant, but filled with electrolyte. Following this speculation, we carried out careful Electron Energy Loss Spectroscopy (EELS) analysis to trace the oxygen signal inside the voids in an NPG dealloyed in concentrated nitric acid, and the results are shown in Figure 4.5. Despite the strong shielding effect from the Au shell, significant oxygen signals absent in other part of the NPG were detected in large encased voids. We believe this is strong evidence that we've obtained a metal-shell / solution-core structure.

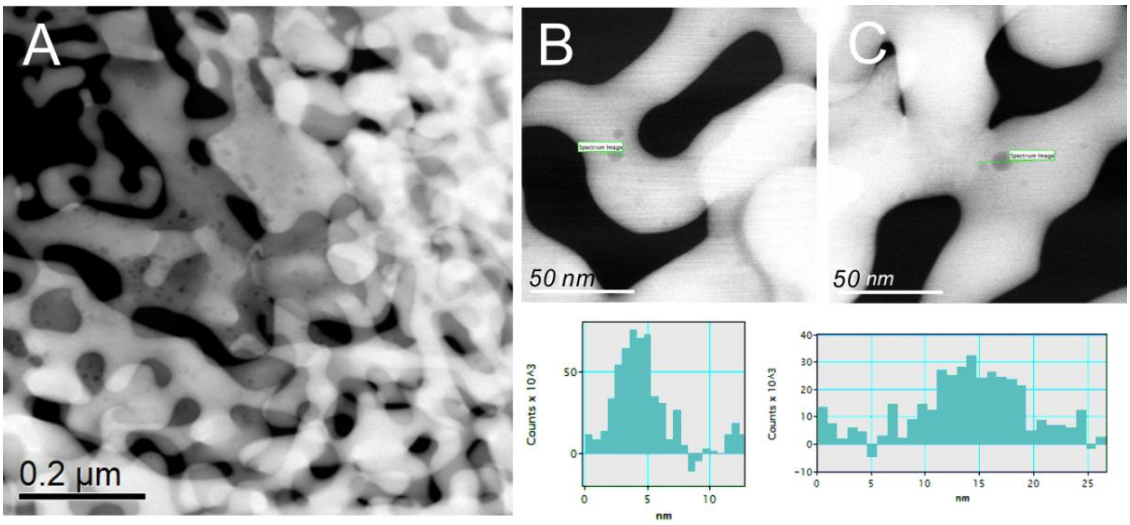

Figure 4.5 (A) Encased voids in NPG and (B, C) EELS scans across voids indicating significantly higher counts of oxygen signals inside the voids

While it may require other characterization methods to confirm the existence of the electrolyte, the structure could have a wide range of applications if realized in a nanoparticle. We note there have been reports on hollow nanoparticle structures prepared by galvanic exchange(*86*, *87*), and although researchers usually refer to bulk diffusion and Kirkendall voiding to explain the morphology, we suspect the so-claimed hollow core should be as well filled with electrolyte.

5 FROM DEALLOYING TO DECOMPOSITION

5.1 Background

So far in my dissertation, I have discussed the behaviors of a broad spectrum of alloys with dramatically different chemical and physical properties. A radical question to pose is that, what if we change one component in the binary alloy to a non-metal For example, what morphology would one observe by selectively removing oxygen from a metal oxide? We will term such a process as decomposition and in analogy to dealloying, vacancy formation should evolve due to component dissolution.

This type of process in fact has been studied before in the electrolysis process, where people realize that without a porous layer formation, electrolysis of metal oxides or halides cannot advance into the bulk solid (*88, 89*). Others have also prepared porous structures in small size scale materials following the argument(*90*). However, no connection has been established between decomposition and dealloying. In this chapter, we will give a preliminary discussion of this process as well as briefly consider the similarities and differences to dealloying.

5.2 The formula of bi-continuous structure evolution from decomposition

Selectively leaching one component from a compound cannot be achieved without a state change of the other. Taking compound A_xB_y (A is a metal element, x and y are both integers) as an example, unlike the dealloying process, the remaining component A is the one with electron transfer, written in the form as

$$A_xB_y + xy\,e^- \rightarrow xA + yB^{x-} \qquad 5\text{-}1$$

Here the compound can be Ag_2S, SnS, or even $CuSO_4$, all of which will be examined later. Due to the limited solid-state conductivities of the compounds, electrochemical decomposition may bring further complications, as the ionic conduction can become the RLS. This problem can be solved by the introduction of reducing agent such as $NaBH_4$ to carry out Reaction 5-1 chemically. The chemical reaction will need to be faster than the solid-state bulk diffusion, because similar as discussed in Chapter 2, if the RLS lies in the shrinking compound phase, the solid / solution interface will not be stable.

While the discussions above are limited to the solid-to-solid phase transition pathway, reactions of solid compounds through corresponding solvated species have been considered to be the dominating paths at least when it comes to electrochemical reductions. For example, $AgCl_n^{(n-1)-}$ always acts as an intermediate ion when AgCl is electrochemically reduced to Ag(*89*, *91*), and the reduction is restrained to the electrolyte / AgCl / Ag triple-phase boundary to provide both the reactants and electrons. Although the location limitation is eliminated in a chemical reaction, the electrolytic pathway could still heavily participate since it often requires lower energy. However, we argue here that the pathways will not affect the general bi-continuous morphology, for the following two reasons. First, the interface will remain macroscopically flat (much larger than the nanoporosity scale) since all the possible RLS's are still in the growing phase. Second, as long as the reducing agent content is much higher than the solvated species, the reduced product will retain its continuity because virtually all reduction will take place in the very vicinity of the interface and the rate and amount of the reduction reaction drops sharply into the electrolyte due to the decreasing reactant concentration.

The electrolytic pathway will in fact give us new ways to control the morphology evolution. In the case of solid-to-solid phase transition like dealloying, the electrode / electrolyte interface stays sharp with the width of an adatom; whereas in the solvation and then reduction process, the interface can be viewed as diffusive. In the view of percolation, a diffusive interface can also be taken as titrating vacancies (filled with electrolyte) of a gradient concentration to dilute down the initial compound composition. An apparent result is that compounds that are initially passive against selective dissolution can be activated to produce bi-continuous structure.

5.3 Experimental

SnS (Precision Chemical), $CuSO_4*5H_2O$ (EMD) and $PbCO_3$ (Alfa Aesar) were used as received. Ag_2S was prepared by oxidizing a Ag wire in 0.1M Na_2S (Sigma Aldrich) solution at 0V vs. NHE. AgO was deposited by applying a fixed current ($0.1mA/cm^2$ to $1mA/cm^2$) to a Pt-Ir wire (ESPI metals) in 0.2M $AgNO_3$ (Sigma Aldrich) and 0.05M NH_4OH (Sigma Aldrich) solution. All the compounds except $CuSO_4*5H_2O$ were reduced by 0.1M $NaBH_4$ (Sigma Aldrich) aqueous solution, and washed with water afterwards. $CuSO_4*5H_2O$ reduction was carried in saturated $NaBH_4$ acetonitrile solution to minimize the compound's solubility, and the product was washed with acetonitrile and water in sequence.

5.4 Results and Discussion

The starting compound morphologies are listed in Figure 5.1. They are all granular in the sense that the size effect we found in dealloying will not enter into the preliminary examinations.

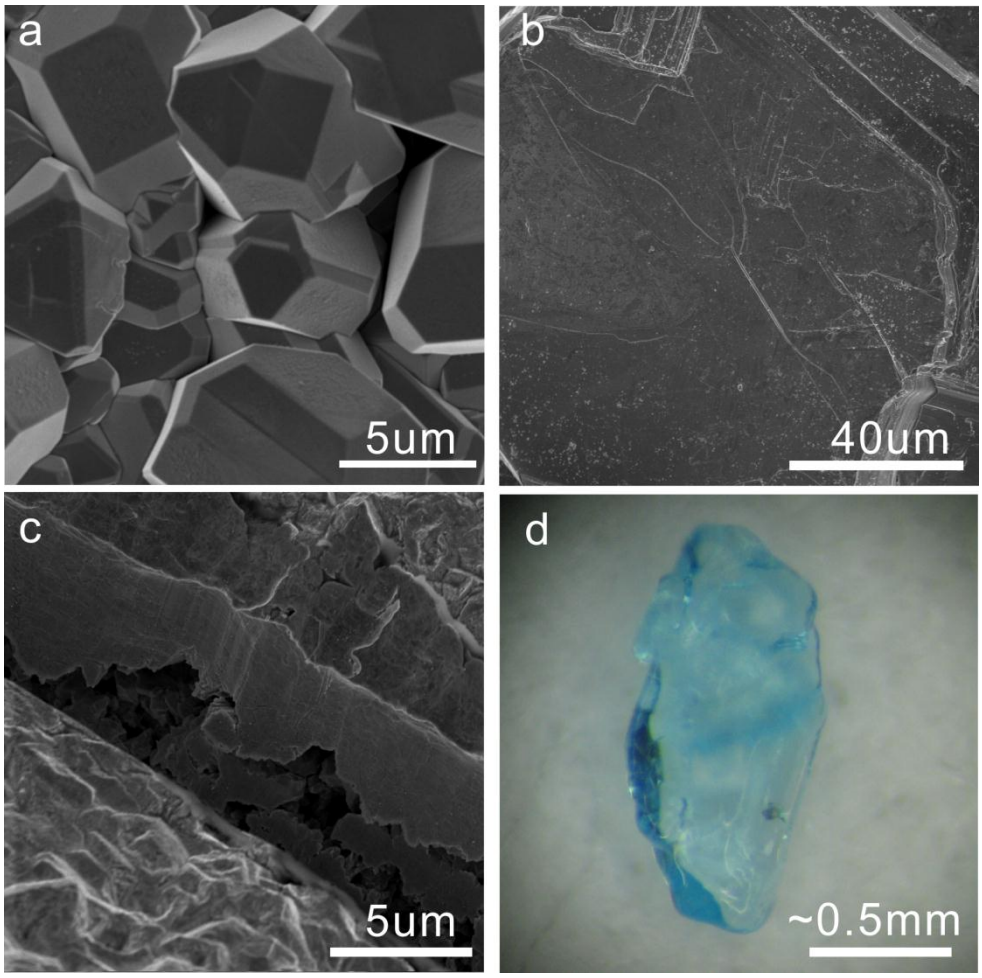

Figure 5.1 Compounds before de-composition reaction, (a) AgO; (b) SnS; (c) Ag_2S (adjacent to a cross-section); (d) $CuSO_4$

As shown in Fig. 5.2, the reductions of both AgO and SnS result in bi-continuous structures almost identical to those obtained by dealloying. The length scales of ligaments also agree perfectly with the points in Figure 4.2, therefore the porous structure coarsening is controlled by the same surface diffusion process. The structures well retain

their initial substrate shapes, indicating most of the phase transition occurred inside the volume of the starting compound; at the same time we believe the electrolytic pathway participated the decomposition process, indicated by the filaments of nanoporous Ag protruding out of the crystalline grains and the rough surface of porous Sn ligaments. Nevertheless, almost no reduction products were found away from the surface, confirming the well-contained decomposition process.

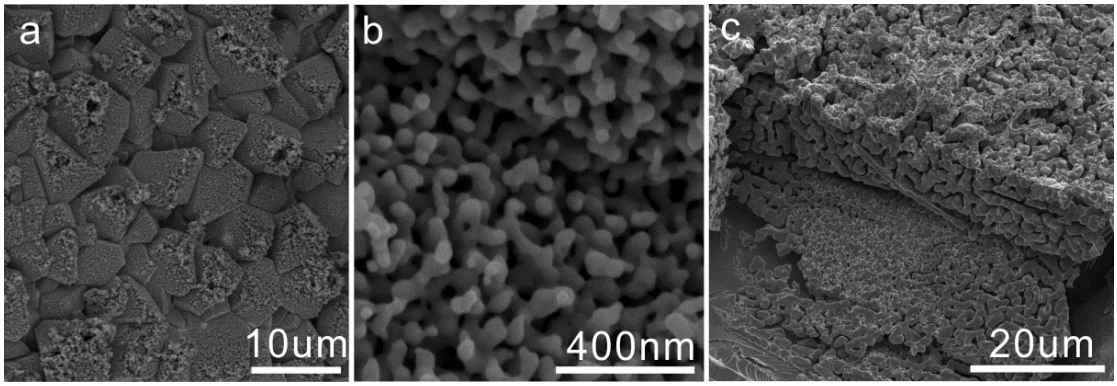

Figure 5.2 Decomposed (a, b) AgO and (c) SnS

The reduction of Ag_2S surprisingly results in well-aligned nanowires instead of bi-continuous structure (Fig. 5.3). The Ag wires are of diameter ranging from 100~200nm, which are comprised of smaller filaments if inspected closely. There are two causes that may be responsible for this type of highly directional structure — the first one is mass transport limitation, and the second is anisotropic growth. We believe the solid-state diffusion in Ag_2S is not playing any role here although the compound is famous for its high ionic conductivity(*92*), because the diffusion rate cannot yield such a reaction depth during the experimental time (~1000s). The anisotropy in the crystal structure could account for the directional decomposition, which will need more investigation, to correlate the packing density of each orientation to the morphology.

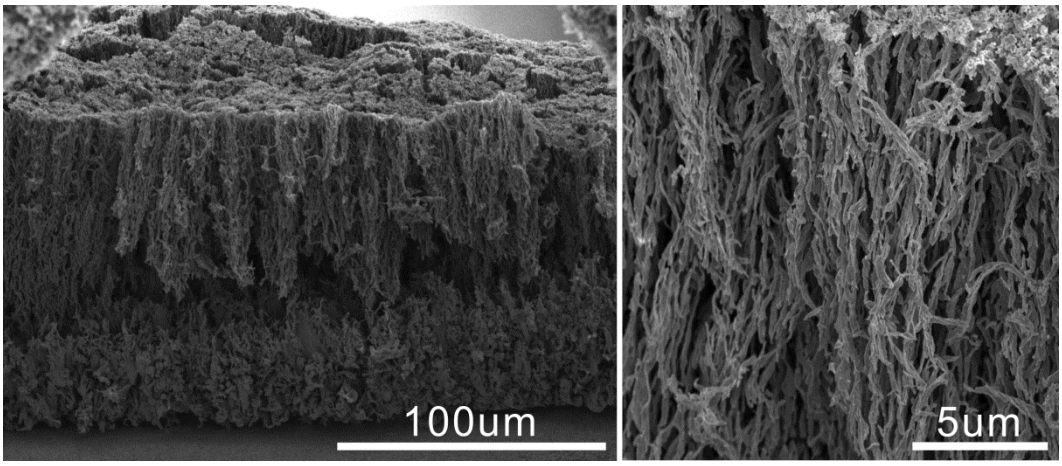

Figure 5.3 Decomposed Ag_2S

At last, we show that the decomposition processes of salts result in same bi-continuous structure. In Figure 5.4, though still covered with precipitates, both reduced $CuSO_4*5H_2O$, and $PbCO_3$ yield porous metal structures that are as bi-continuous as dealloying products. The ligament sizes again agree with the prediction in Figure 4.2. These results extend the applicability of the decomposition process to a huge volume of chemicals, therefore give the possibility to further tune the involved parameters like reactant solubility to study their effects on morphology evolution. Moreover, the paths towards nanoporous structures become abundant, which greatly benefits the control of morphology as well as the cost of fabrication.

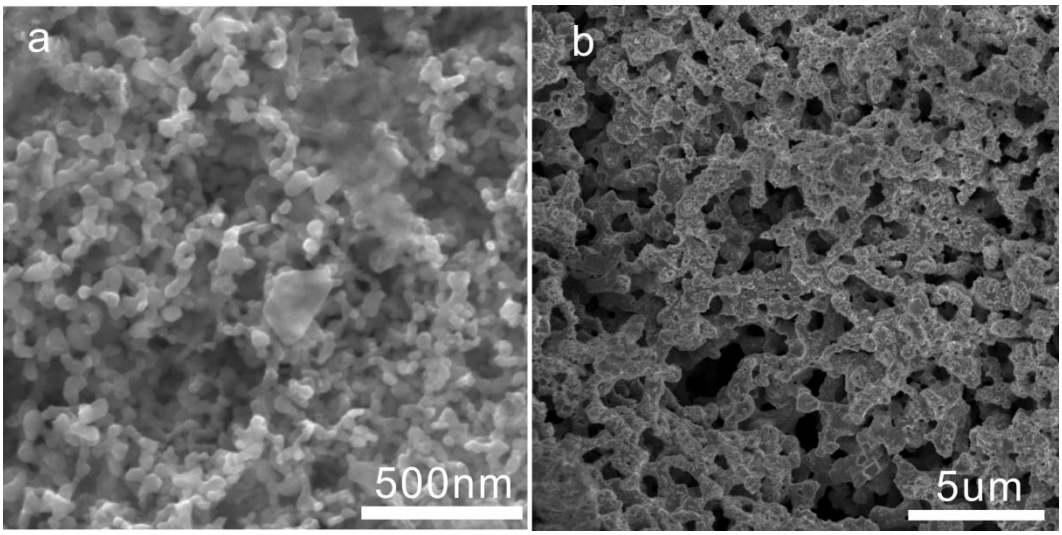

Figure 5.4 Decomposed (a) $CuSO_4*5H_2O$, (b) $PbCO_3$

6 CONCLUSIONS

1. In a bulk electrode, at sufficiently high overvoltage, regardless of the rate of solid-state bulk diffusivity, dealloying always results in bi-continuous porous structure as long as the less noble component composition is above the parting limit.
2. The length scale of the porous metal, i.e. ligament diameter, is controlled by surface diffusion, and can be correlated empirically to the homologous temperature.
3. If the less noble component content goes below the parting limit, especially the percolation threshold, negative void dendrite structure should evolve during the bulk diffusion controlled dealloying, unless surface diffusion rate is too high or grain boundary diffusion dominates, in the case of which dealloying produces only surface roughness. Kirkendall voiding always occurs along with bulk diffusion controlled dealloying.
4. The negative dendrite shapes will be anisotropic if the more noble component possesses anisotropic surface energy.
5. There exist a critical size for particulate alloy electrode to contain porosity evolution, which is usually 2~3 times of the “steady-state” ligament size.
6. Under conditions for which lattice diffusion is significant, low dealloying rate will not result in bi-continuous owing to the evolution of a surface layer rich in the more noble component. Dealloying proceeds thorough this layer supported by solid-state transport.
7. Enclosed voids observed inside NPG ligaments, induced by Rayleigh instability, contain electrolyte trapped during the surface diffusion controlled encapsulation.

8. The correlation between morphology and its controlling kinetics in dealloying can be extended beyond dealloying, to other interfacial controlled morphology evolution. For example, selective dissolution of elemental components in compounds can result in bi-continuous structures as well.

REFERENCES

1. G. Tammann, *Anorg. Allg. Chem* **118**, 293–308 (1921).

2. G. Borelius, *Ann. Phys. (Berlin)* **379**, 216–230 (1924).

3. H. Pickering, *Corros. Sci.* **23**, 1107–1120 (1983).

4. K. Sieradzki *et al.*, *J. Electrochem. Soc.* **149**, B370–B377 (2002).

5. R. C. Newman, K. Sieradzki, *Science* **263**, 1708–1709 (1994).

6. K. Sieradzki, *J. Electrochem. Soc.* **134**, 1635 (1987).

7. K. Sieradzki, R. Newman, *J. Phys. Chem. Solids* **48**, 1101–1113 (1987).

8. J. Snyder, T. Fujita, M. W. Chen, J. Erlebacher, *Nat. Mater.* **9**, 904–907 (2010).

9. K. Hu, D. Lan, X. Li, S. Zhang, *Anal. Chem.* **80**, 9124–30 (2008).

10. J. Biener *et al.*, *Nat. Mater.* **8**, 47–51 (2009).

11. E. M. Bringa *et al.*, *Nano Lett.* **12**, 3351–3355 (2012).

12. R. Li, K. Sieradzki, *Phys. Rev. Lett.* **68**, 1168–1171 (1992).

13. A. Dursun, D. V. Pugh, S. G. Corcoran, *J. Electrochem. Soc.* **152**, B65 (2005).

14. K. Wagner, S. R. Brankovic, N. Dimitrov, K. Sieradzk, *J. Electrochem. Soc.* **144**, 3545 (1997).

15. H. W. Pickering, C. Wagner, *J. Electrochem. Soc.* **114**, 698–706 (1967).

16. W. Mallard, A. Gardner, R. F. Bass, L. Slifkin, *Phys. Rev.* **129**, 617 (1963).

17. H. Kaesche, *Metallic Corrosion: Principles of Physical Chemistry and Current Problems* (NACE, Houston, TX, ed. 2nd, 1985), pp. 194–211.

18. A. Forty, *Nature* **282**, 597–598 (1979).

19. K. Sieradzki, R. Corderman, K. Shukla, R. C. R. Newman, *Philos. Mag.* **59**, 713–746 (1989).

20. K. Sieradzki, *Journal of Physical C: Solid State Physics* **18**, 855–857 (1985).

21. D. Stauffer, A. Aharony, *Introduction to Percolation Theory* (Taylor & Francis, ed. 2nd, 1992).

22. J. Rugolo, J. Erlebacher, K. Sieradzki, *Nat. Mater.* **5**, 946–949 (2006).

23. J. Erlebacher, M. Aziz, A. Karma, N. Dimitrov, K. Sieradzki, *Nature* **410**, 450–453 (2001).

24. Y. Ding, M. Chen, *MRS bulletin* **34**, 567–576 (2009).

25. Y. Yu *et al.*, *Nano Lett.* (2012), doi:10.1021/nl203920s.

26. Q. Zhang, Z. Zhang, *Physical chemistry chemical physics : PCCP* **12**, 1453–72 (2010).

27. M. Oezaslan, M. Heggen, P. Strasser, *J. Am. Chem. Soc.* **134**, 514–24 (2012).

28. Z. Zhang *et al.*, *J. Mater. Chem.* **19**, 6042 (2009).

29. F.-H. Yeh, C.-C. Tai, J.-F. Huang, I.-W. Sun, *J. Phys. Chem. B* **110**, 5215–22 (2006).

30. J. Yu *et al.*, *Chem. Mater.* **20**, 4548–4550 (2008).

31. J. Snyder, I. McCue, K. Livi, J. Erlebacher, *J. Am. Chem. Soc.* **134**, 8633–8645 (2012).

32. J. Erlebacher, *J. Electrochem. Soc.* **151**, C614 (2004).

33. D. M. Artymowicz, J. Erlebacher, R. C. Newman, *Philos. Mag.* **89**, 1663–1693 (2009).

34. J. Erlebacher, *Phys. Rev. Lett.* **106**, 1–4 (2011).

35. I. McCue *et al.*, *Phys. Rev. Lett.* **108**, 1–5 (2012).

36. K. Kolluri, M. J. Demkowicz, *Acta Mater.* **59**, 7645–7653 (2011).

37. J. Greeley, J. Norskov, *Electrochim. Acta* **52**, 5829–5836 (2007).

38. P. Buffat, J. Borel, *Phys. Rev. A.* **13**, 2287–2298 (1976).

39. K. Dick, T. Dhanasekaran, Z. Zhang, D. Meisel, *J. Am. Chem. Soc.* **124**, 2312–7 (2002).

40. R. A. Huggins, *J. Power Sources* **81-82**, 13–19 (1999).

41. C. Wagner, *J. Electrochem. Soc.* **103**, 571–580 (1956).

42. J. Harrison, C. Wagner, *Acta Metallurgica* **7**, 722 (1959).

43. H. Kaiser, *Corrosion science* **34**, 683–699 (1993).

44. J. Cahn, *Acta Metallurgica* **28**, 1333–1338 (1980).

45. F. Larche, J. Cahn, *Acta Metallurgica* **33**, 331–357 (1985).

46. D. Schmatz, H. Domian, H. Aaronson, *Transactions Of the Metallurgical Society of AIME* **236**, 543–554 (1966).

47. M. Hansen, K. Anderko, *Constitution of Binary Alloys* (McGraw- Hill, 1958).

48. D. Tromans, *J. Electrochem. Soc.* **156**, C367 (2009).

49. C. D. Lorenz, R. May, R. M. Ziff, *Journal of Statistical Physics* **98**, 961–970 (2000).

50. M. Liu, D. Qiu, M.-C. Zhao, G. Song, A. Atrens, *Scr. Mater.* **58**, 421–424 (2008).

51. R. S. Lillard, G. F. Wang, M. I. Baskes, *J. Electrochem. Soc.* **153**, B358 (2006).

52. M. Methfessel, D. Hennig, M. Scheffler, *Phys. Rev. B* **46**, 4816–4829 (1992).

53. H. Kirchner, G. Chadwick, *Philos. Mag.* **20**, 405–411 (1969).

54. K. Weichert *et al.*, *J. Am. Chem. Soc.* **134**, 2988–92 (2012).

55. M. Winter, J. O. Besenhard, *Electrochim. Acta* **45**, 31–50 (1999).

56. S.-C. Chao *et al.*, *J. Phys. Chem. C* **111**, 22040–22047 (2011).

57. J. W. Choi *et al.*, *Nano Lett.* **10**, 1409–13 (2010).

58. X. H. Liu *et al.*, *Nano Lett.* **11**, 3991–3997 (2011).

59. A. D. W. Todd, P. P. Ferguson, M. D. Fleischauer, J. R. Dahn, *Int. J. Energy Res.* **34**, 535–555 (2010).

60. A. J. Bard, L. R. Faulkner, *Electrochemical Methods: Fundamentals and Applications* (Wiley, Hoboken, NJ, ed. 2nd, 2000), pp. 228–231.

61. S. Yang, P. Y. Zavalij, M. S. Whittingham, *Electrochem. Commun.* **5**, 587–590 (2003).

62. J. Hassoun, S. Panero, B. Scrosati, *Int. J. Electrochem. Sci.* **1**, 110–121 (2006).

63. J. Weissmüller, R. C. Newman, H. Jin, A. M. Hodge, J. W. Kysar, *MRS Bulletin* **34**, 577–586 (2009).

64. I. C. Oppenheim, D. J. Trevor, C. E. Chidsey, P. L. Trevor, K. Sieradzki, *Science* **254**, 687–9 (1991).

65. F. Renner, A. Stierle, H. Dosch, D. Kolb, *Nature* **439**, 707–710 (2006).

66. X. Li, thesis, Arizona State University (2012).

67. C. Carlton, S. Chen, P. Ferreira, *Journal of Physical Chemistry Letters* **3**, 161–167 (2012).

68. H. L. Xin *et al.*, *Nano Lett.* **12**, 490–7 (2012).

69. A. Dursun, D. V. Pugh, S. G. Corcoran, *J. Electrochem. Soc.* **150**, B355 (2003).

70. L. H. Qian, M. W. Chen, *Appl. Phys. Lett.* **91**, 083105 (2007).

71. Y. K. Chen-Wiegart *et al.*, *Acta Mater.* **60**, 4972–4981 (2012).

72. H. Rösner, S. Parida, D. Kramer, C. a. Volkert, J. Weissmüller, *Adv. Eng. Mater.* **9**, 535–541 (2007).

73. J. Snyder, J. Erlebacher, *J. Electrochem. Soc.* **157**, C125 (2010).

74. S. G. Corcoran, D. G. Wiesler, K. Sieradzki, *MRS Proceedings* **451**, 93–98 (1996).

75. J. Snyder, K. Livi, J. Erlebacher, *J. Electrochem. Soc.* **155**, C464 (2008).

76. C. P. Flynn, *J. Phys.: Condens. Matter* **18**, S439–S445 (2006).

77. W. W. Mullins, *J. Appl. Phys.* **30**, 77 (1959).

78. S. Sun, thesis, Arizona State University (2012).

79. J. Hayes, A. Hodge, J. Biener, *J. Mater. Res.* **21**, 2611–2616 (2006).

80. M. Hakamada, M. Mabuchi, *J. Alloys Compd.* **479**, 326–329 (2009).

81. C. Xu, Y. Li, F. Tian, Y. Ding, *ChemPhysChem* **11**, 3320–8 (2010).

82. N. A. Senior, R. C. Newman, *Nanotechnology* **17**, 2311–2316 (2006).

83. S. Parida *et al.*, *Phys. Rev. Lett.* **97**, 4–7 (2006).

84. F. Nicholas, W. Mullins, *Transactions Of the Metallurgical Society of AIME* **233**, 1840 (1965).

85. F. Nichols, *J. Nucl. Mater.* **148**, 92–98 (1987).

86. J. X. Wang *et al.*, *J. Am. Chem. Soc.* **133**, 13551–7 (2011).

87. S. J. Bae *et al.*, *J. Mater. Chem.* **22**, 8820 (2012).

88. G. Chen, D. Fray, T. Farthing, *Nature* **407**, 361–4 (2000).

89. W. Xiao, X. Jin, Y. Deng, D. Wang, G. Z. Chen, *Chemistry (Weinheim an der Bergstrasse, Germany)* **13**, 604–12 (2007).

90. G. R. Bourret, P. J. G. Goulet, R. B. Lennox, *Chem. Mater.* **23**, 4954–4959 (2011).

91. T. Katan, S. Szpak, D. N. Bennion, *J. Electrochem. Soc.* **121**, 757 (1974).

92. C. Wagner, *J. Chem. Phys.* **21**, 1819 (1953).